Astronomy & Astrophysics manuscript no. jmparedes
September 3, 2009

Radio continuum and near-infrared study of the MGRO J2019+37 region

J.M. Paredes[1], J.Martí[2,3], C.H. Ishwara-Chandra[4], J.R. Sánchez-Sutil[3], A.J. Muñoz-Arjonilla[2,3], J. Moldón[1], M. Peracaula[5], P.L. Luque-Escamilla[3], V. Zabalza[1], V. Bosch-Ramon[6], P. Bordas[1], G.E. Romero[7,8]⋆, and M. Ribó[1]

[1] Departament d'Astronomia i Meteorologia and Institut de Ciències del Cosmos (ICC), Universitat de Barcelona (UB/IEEC), Martí i Franquès 1, 08028 Barcelona, Spain
e-mail: jmparedes@ub.edu, jmoldon@am.ub.es, vzabalza@am.ub.es, pbordas@am.ub.es, mribo@am.ub.es
[2] Departamento de Física, EPS, Universidad de Jaén, Campus Las Lagunillas s/n, Edif. A3, 23071 Jaén, Spain
e-mail: jmarti@ujaen.es, ajmunoz@ujaen.es
[3] Grupo de Investigación FQM-322, Universidad de Jaén, Campus Las Lagunillas s/n, Edif. A3, 23071 Jaén, Spain
e-mail: jrssutil@ujaen.es, peter@ujaen.es
[4] NCRA, TIFR, Post Bag 3, Ganeshkhind, Pune-411 007, India
e-mail: ishwar@ncra.tifr.res.in
[5] Institut d'Informàtica i Aplicacions, Universitat de Girona, Girona, Spain
e-mail: marta.peracaula@udg.edu
[6] Max Planck Institut für Kernphysik, Saupfercheckweg 1, Heidelberg 69117, Germany
e-mail: vbosch@mpi-hd.mpg.de
[7] Instituto Argentino de Radioastronomía (CCT La Plata, CONICET), C.C.5, (1894) Villa Elisa, Buenos Aires, Argentina
e-mail: romero@iar.unlp.edu.ar
[8] Facultad de Ciencias Astronómicas y Geofísicas, UNLP, Paseo del Bosque, 1900 La Plata, Argentina
e-mail: romero@fcaglp.unlp.edu.ar

Received / Accepted

ABSTRACT

Context. MGRO J2019+37 is an unidentified extended source of very high energy gamma-rays originally reported by the Milagro Collaboration as the brightest TeV source in the Cygnus region. Its extended emission could be powered by either a single or several sources. The GeV pulsar AGL J2020.5+3653, discovered by AGILE and associated with PSR J2021+3651, could contribute to the emission from MGRO J2019+37.
Aims. Our aim is to identify radio and near-infrared sources in the field of the extended TeV source MGRO J2019+37, and study potential counterparts to explain its emission.
Methods. We surveyed a region of about 6 square degrees with the Giant Metrewave Radio Telescope (GMRT) at the frequency 610 MHz. We also observed the central square degree of this survey in the near-infrared $K_{\rm s}$-band using the 3.5 m telescope in Calar Alto. Archival X-ray observations of some specific fields are included. VLBI observations of an interesting radio source were performed. We explored possible scenarios to produce the multi-TeV emission from MGRO J2019+37 and studied which of the sources could be the main particle accelerator.
Results. We present a catalogue of 362 radio sources detected with the GMRT in the field of MGRO J2019+37, and the results of a cross-correlation of this catalog with one obtained at near-infrared wavelengths, which contains $\sim 3\times10^5$ sources, as well as with available X-ray observations of the region. Some peculiar sources inside the $\sim1^\circ$ uncertainty region of the TeV emission from MGRO J2019+37 are discussed in detail, including the pulsar PSR J2021+3651 and its pulsar wind nebula PWN G75.2+0.1, two new radio-jet sources, the H II region Sh 2-104 containing two star clusters, and the radio source NVSS J202032+363158. We also find that the hadronic scenario is the most likely in case of a single accelerator, and discuss the possible contribution from the sources mentioned above.
Conclusions. Although the radio and GeV pulsar PSR J2021+3651 / AGL J2020.5+3653 and its associated pulsar wind nebula PWN G75.2+0.1 can contribute to the emission from MGRO J2019+37, extrapolation of the GeV spectrum does not explain the detected multi-TeV flux. Other sources discussed here could contribute to the emission of the Milagro source.

Key words. gamma-rays: observations – H II regions – infrared: stars – radio continuum: stars – X-rays: binaries

1. Introduction

The Galactic very-high-energy (VHE) γ-ray sources discovered by the latest generation of Cherenkov observatories (H.E.S.S., MAGIC, Milagro) are currently an actively studied topic in modern high-energy astrophysics. Among the ~75 detected sources, nearly one third remain yet as unidentified. A significant number of them have extended morphologies on 0.1–1° scales in the TeV energy band, ensuring that the identification of counterparts at lower energies is a very difficult task. The most representative of this new population of Galactic sources is TeV J2032+4130, inside whose error box both compact and extended radio sources on arcsecond scales were found (Paredes et al. 2007). *XMM-Newton* observations of this source also detected faint extended X-ray emission (Horns et al. 2007a).

⋆ Member of CONICET

An addition to the population of extended, unidentified TeV sources was reported by the Milagro collaboration, following the discovery in the Cygnus region of the most extended TeV source known so far (Abdo et al. 2007a,b). The TeV emission from this area covers several square degrees and includes diffuse emission and at least one new source, MGRO J2019+37, located to within an accuracy of ±0.4°. After the Crab Nebula, MGRO J2019+37 is the strongest source detected by Milagro. The Tibet AS-γ experiment confirmed the detection of this source by measuring a 5.8σ signal compatible with the position of MGRO J2019+37 (Amenomori et al. 2008). On the other hand, VERITAS inferred an upper limit that is compatible with the Milagro detection for a hard-spectrum extended source (Kieda et al. 2008).

The origin of all these types of emission and their association with astrophysical sources is unclear. Although a possible connection with the anisotropy of Galactic cosmic rays was proposed (Amenomori et al. 2006), the TeV γ-ray flux measured at 12 TeV from the diffuse emission of the Cygnus region (after excluding MGRO J2019+37), exceeds that predicted by a conventional model of cosmic ray production and propagation (Abdo et al. 2007a). This strongly infers the existence of hard-spectrum cosmic-ray sources and/or other types of TeV γ-ray sources in the region. It is unclear whether the emission originates in either a single extended source or a combination of several point sources. MGRO J2019+37 is positionally coincident with the EGRET sources 3EG J2021+3716 and 3EG J2016+3657 (see Fig. 1). These sources could represent the GeV counterparts to the TeV source MGRO J2019+37, which may be a multiple source. Only one of them, 3EG J2021+3716, appears in the bright gamma-ray source list published by the *Fermi Gamma-ray Space Telescope* (Abdo et al. 2009). Previous observations with *AGILE* illustrated its pulsar nature and inferred an association of this source with PSR J2021+3651 (Halpern et al. 2008).

To explain steady VHE γ-ray emission, hadronic models have been developed by several authors (e.g., Aharonian & Atoyan 1996; Butt et al. 2003; Torres et al. 2004; Bordas et al. 2009). The electromagnetic radiation produced by both hadronic jets from microquasars and Galactic cosmic rays, and their interaction with the ISM were explored by Bosch-Ramon et al. (2005). The interaction between the high energy protons, accelerated at the jet termination shock, and the interstellar hydrogen nuclei produces charged and neutral pions (π^-, π^+ and π^0); the first set will decay to electrons and positrons and the second set to photons. The primary radiation, π^0-decay photons, is in the γ-ray band, but the secondary particles can produce significant fluxes of synchrotron (from radio frequencies to X-rays) and bremsstrahlung emission (from soft γ-rays to the TeV range), and in general lower efficiency, inverse Compton (IC) emission by interaction with ambient infrared photons. Detectable fluxes of extended and steady emission should be produced by this mechanism. Other scenarios involve a jet-driven termination shock at which relativistic electrons produce synchrotron and TeV IC emission (Aharonian & Atoyan 1998). In this context, X-ray observations provide a crucial constraint of the IC emission.

To understand the nature of the Milagro source in the Cygnus region, we performed a multiwavelength campaign comprising a deep radio survey at 610 MHz using the Giant Metrewave Radio Telescope (GMRT) interferometer covering the 3.5°×3.5° MGRO J2019+37 field, near-infrared observations in the K_s band using the 3.5 m telescope at Calar Alto of the central square degree, and archival X-ray data.

This paper is organized as follows. In Sect. 2, we report on previous radio surveys of the Cygnus region, while in Sect. 3 we present the GMRT survey and the results obtained. In Sect. 4, we provide an overview of the near-infrared survey, and in Sect. 5 we report on the cross-correlations both between our GMRT survey and the near-infrared survey, and between the GMRT survey and previous X-ray observations. We comment on particularly interesting sources in Sect. 6 and we discuss their possible contribution to the TeV emission of MGRO J2019+37 in Sect. 7. We finish with our conclusions in Sect. 8.

2. Previous radio surveys of the Cygnus region

At radio frequencies, the Cygnus region has been imaged many times, sometimes as part of Galactic surveys. However, these studies were carried out at poor angular resolution and/or a relatively high limiting flux density. Some of the most representative of previous surveys are: the Canadian Galactic Plane Survey (CGPS) performed with the Synthesis Telescope at the Dominion Radio Astrophysical Observatory (DRAO) at 408 and 1420 MHz, with angular resolutions of 5.′3 and 1.′6, and limiting flux densities of 9 and 1 mJy, respectively, at declination of +40° (Taylor et al. 2003); the Westerbork Synthesis Radio Telescope (WSRT) 327 MHz survey with an angular resolution of 1′ and a limiting flux density of 10 mJy (Taylor et al. 1996); and the DRAO 408 and 1430 MHz survey with angular resolution of 3.5′×5.2′ and 1.0′×1.5′, respectively, and limiting flux densities of 150 and 45 mJy, respectively (Wendker et al. 1991). The most recent survey of this region is the WSRT 350 and 1400 MHz continuum survey of the Cygnus OB2 association, with angular resolutions of 55″ and 13″, and limiting flux densities of 10–15 and 2 mJy, respectively (Setia Gunawan et al. 2003). The WSRT survey does not cover the MGRO J2019+37 field.

3. GMRT 610 MHz Radio Survey

3.1. Observations

The MGRO J2019+37 region was observed with wide-field deep radio imaging at 610 MHz (49 cm) using the GMRT, located in Pune (India). We designed an hexagonal pattern of 19 pointings to cover the region of about 2.5°×2.5° centred on the MGRO J2019+37 peak of emission. The observations were carried out in July 2007, but were affected by a series of power failures in the array and compensatory time was scheduled in August 2007.

The flux density scale was set using the primary amplitude calibrators 3C 286 and 3C 48, which were observed at the beginning and end of each observing session. On the other hand, phase calibration was performed by repeated observations of the nearby phase calibrator J2052+365. Each pointing was observed for a series of scans to achieve a good coverage in the *uv* plane, the total time spent on each field being 45 minutes. The total effective time amounts to 20 hours.

Observations were made in two 16-MHz upper and lower sidebands (USB and LSB) centered on 610 MHz, each divided into 128 spectral channels. The data of each side-band were separately edited with standard tasks of the Astronomical Image Processing System (`AIPS`) package. There were no major radio frequency interference (RFI) problems. However, we did find that narrow band RFI affected a few channels across the band, which were completely flagged. Once poor antennas, baselines, or channels were removed, the bandpass correction was used to extend the calibration to all channels. After the bandpass calibration, the central channels of each sideband were averaged, leading to a data file of 5 compressed channels, of a bandwidth small

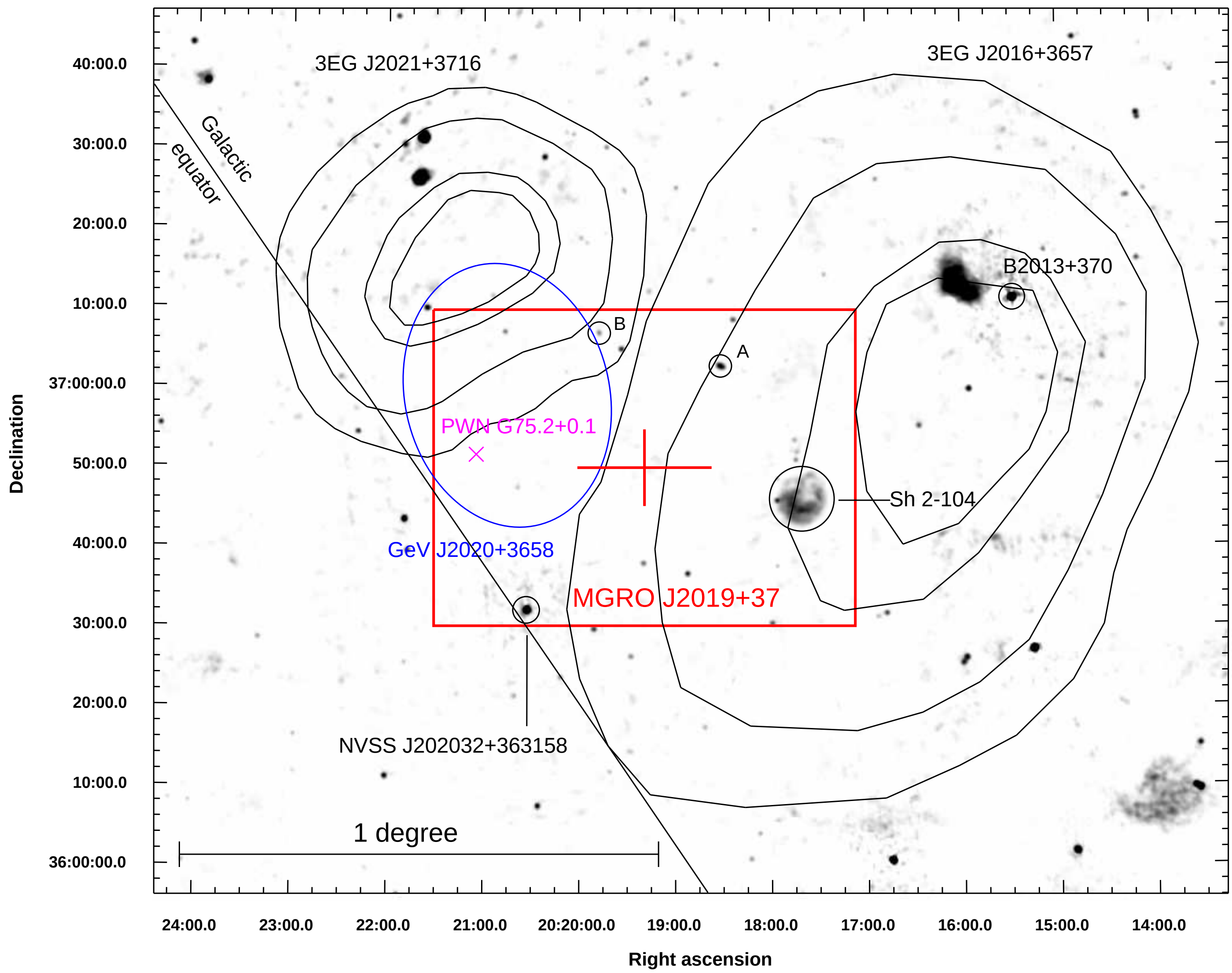

Fig. 1. Radio map obtained with the GMRT at 610 MHz (greyscale) convolved with a circular restoring beam of 30″. The red cross and box indicate the center of gravity and its positional uncertainty including statistic and systematic errors of the TeV emission from the source MGRO J2019+37 (Abdo et al. 2007b). The conspicuous radio sources located inside this box correspond to the extended H II region Sh 2-104, a bright compact radio source also detected with the VLA as NVSS J202032+363158, and two newly discovered jet-like sources (A and B). The position probability contours (50%, 68%, 95%, and 99%, from inside to outside) of the Third EGRET catalogue sources 3EG J2021+3716 and 3EG J2016+3657 (Hartman et al. 1999), as well as the GeV source GeV J2020+3658 (blue ellipse) (Lamb & Macomb 1997) are superimposed. The magenta cross indicates the position of the pulsar wind nebula PWN G75.2+0.1. The blazar B2013+370 within 3EG J2016+3657 is also labeled.

enough to avoid bandwidth smearing problems in our images. Standard calibration for continuum data was performed beyond this point. At the end of the self-calibration deconvolution iteration scheme, we combined both USB and LSB images of each pointing and mosaicked the entire region using the `AIPS` task `FLATN`.

We produced different maps of between high and low angular resolution of the GMRT mosaic. Our highest quality image has an rms of 0.2 mJy beam^{-1} with a 5″ resolution because of the long baselines of the GMRT. A low angular resolution version was also produced using a restoring beam of 30″ to enhance the extended radio sources in the field. This map has an rms of 0.5 mJy beam^{-1}.

3.2. Results

Figure 1 shows a low angular resolution radio image of the MGRO J2019+37 field, together with the position of sources at other wavelengths. The location of MGRO J2019+37 is consistent with those of the EGRET sources 3EG J2016+3657 and 3EG J2021+3716. The first of them is positionally coincident with the blazar-like source B2013+370 (G74.87+1.22) (Mukherjee et al. 2000; Halpern et al. 2001), although this blazar is well outside the inner box of MGRO J2019+37. The second is marginally coincident with the pulsar wind nebula PWN G75.2+0.1 (Hessels et al. 2004). High-energy gamma-ray pulsations originating in the pulsar were detected by *AGILE* and *Fermi* (Halpern et al. 2008; Abdo et al. 2009). There are other known strong and/or extended radio sources in the field, such as the brightest one inside the MGRO J2019+37 center of gravity box, NVSS J202032+363158, and the H II region Sh 2-104 (also

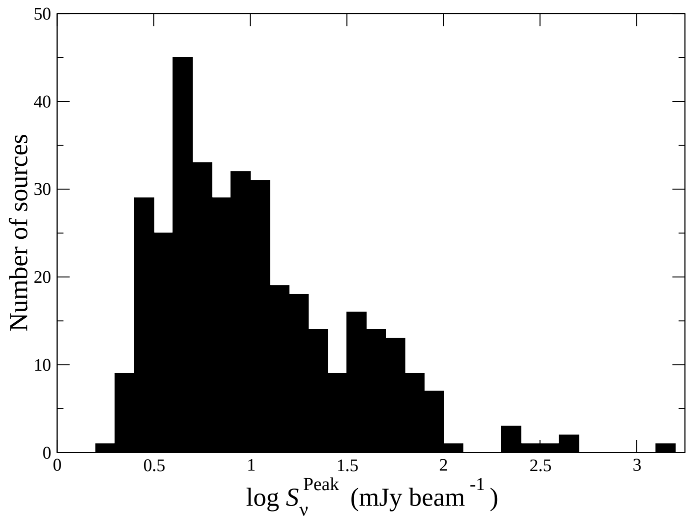

Fig. 2. Number of sources versus log $S_\nu^{\rm Peak}$ for the 362 sources detected in the GMRT 610 MHz radio survey.

known as Sh 104). Other interesting sources not obvious at first glance become evident when considering the whole field in detail. Some of them display a resolved morphology, and in Sect. 6 we discuss these objects in more detail.

3.3. Radio catalogue

We applied the `SEXtractor` automatic procedure (Bertin & Arnouts 1996) to our 5″ resolution mosaic (with pixel size of 1″) to produce a list of sources with peak flux density higher than about ten times the local noise after primary beam correction. Objects with less than 5 connected pixels above the threshold were not included. The output was visually inspected and all candidate detections inferred to be false (i.e., deconvolution artifacts near bright sources) were simply deleted by hand. We used the local background analysis in SEXtractor to take into account the uneven background because of beam response effects. Considering the 5″ beam size of the mosaic that we used, and the signal-to-noise ratio that we required for detection, we estimate that the positions obtained have a typical uncertainty of 0.″5 or smaller.

The resulting list, considered to be very reliable although not complete at the lowest flux density levels, contains 362 radio sources. Among them, 203 are fainter than 10 mJy and the majority were previously undetected at radio wavelengths. We present the catalogue in Table 2 of the online material accompanying this paper. The first and second columns provide the catalogue number and the source name. The third and fourth columns give the J2000.0 position in right ascension order. The fifth and sixth columns provide the peak flux density and the local noise, respectively. The seventh and eighth columns list the integrated flux density and its error. Uncertainties quoted for the peak and integrated flux densities are based on the formal errors of the fit and allow the reliability of the detection to be judged. However, they do not include the error due to primary beam correction as a function of angular distance to the phase centre because of unknown antenna offsets, which is estimated to be around 10% of the flux density values (see for instance Paredes et al. 2008). In Fig. 2, we show the source distribution histogram as a function of log $S_\nu^{\rm Peak}$.

4. Near-infrared survey

We also carried out a near-infrared (NIR) survey of the central square degree of the region using the OMEGA2000 wide field camera (15′ × 15′) on the 3.5 m telescope at Centro Astronómico Hispano Alemán (CAHA) in Calar Alto (Spain) on 25 September 2007. This instrument consists of a Rockwell HAWAII2 HgCdTe detector with 2048 × 2048 pixels sensitive from 0.8 to 2.5 μm. The observations were performed in the $K_{\rm s}$-band (2.15 μm) to minimize the interstellar absorption. Individual frames were sky-subtracted, flat-field corrected, and then combined into a final mosaic using the `AIPS` task `FLATN`. The ensamble of 4 × 4 pointings covers almost completely the center of gravity and uncertainty region of the TeV emission from the source MGRO J2019+37. The average limiting magnitude across the mosaic is $K_{\rm s} \simeq 17$ mag, and the total field of view is 0.9° × 0.9°. Astrometric solutions for the final frames were determined within ±0.″1 by identifying about twenty reference stars in each pointing, for which positions were retrieved from the 2MASS catalogue (Skrutskie et al. 2006). A catalogue of ∼315 000 near-infrared sources was produced using the SEXtractor package.

5. Radio, near-infrared, and X-ray cross-correlation catalogue

We performed a cross-correlation between the radio and near-infrared source catalogues. Considering the 0.″5 uncertainty in the radio positions and the 0.″1 uncertainty in the NIR ones, we used a conservative maximum offset of 0.″6 for associations (neglecting systematics between both catalogues). There are 42 of the 362 detected radio sources inside the area imaged in the near infrared. A total of 6 of these 42 sources have a near-infrared counterpart candidate within 0.″6 of their radio position. Their magnitudes are listed in the ninth column of Table 2 of the online material. The chance coincidence probability of finding a NIR source closer than 0.″6 to a given radio source is estimated to be the number of NIR sources multiplied by the area of the uncertainty in positions occupied by the 42 radio sources, divided by the total area of the region: $(315\,000 \times 42\ \pi\ 0.''6^2)/(3240'' \times 3240'') = 1.4$. Therefore, of the six radio sources with NIR counterpart, we expect that one of them is a random coincidence.

We also obtained source lists of all X-ray observations of the region performed by *Chandra* and *XMM-Newton*, computed by the `celldetect` and `edetect_chain` tasks from CIAO 4.0 and SAS 8.0, respectively. A total of 41 of the 362 radio sources are located in fields observed in X-rays, which cover an area of 314 arcmin^2 (1 130 973 arcsec^2) and contain 519 X-ray sources. We found that 5 of the 41 radio sources have an X-ray counterpart candidate within 5″ (the typical uncertainty for *XMM-Newton*). Their X-ray fluxes are listed in the tenth column of Table 2 of the online material. The chance coincidence probability of finding a radio source closer than 5″ to a given X-ray source is estimated to be the number of radio sources multiplied by the area of the uncertainty in positions occupied by the 5 X-ray sources, divided by the total area of the region: $(41 \times 519\ \pi\ 5''^2)/(1\,130\,973\ {\rm arcsec}^2) = 1.4$. Therefore, of the five X-ray sources with radio counterpart we also expect that one of them is a random coincidence.

A single triple radio/near-infrared/X-ray coincidence has been found (source number 115 in Table 2 of the online material).

6. Individual sources in the MGRO J2019+37 field

The most interesting radio sources that appear in the uncertainty region of the TeV emission (red box in Fig. 1) are described below.

6.1. PSR J2021+3651 / PWN G75.2+0.1

The radio pulsar PSR J2021+3651 has a rotation period $P = 0.104$ s, a characteristic age of $P/2\dot{P} = 17$ kyr, and a spin-down luminosity $\dot{E} = 3.4 \times 10^{36}$ erg s^{-1}. It is coincident with the unidentified source GeV 2020+3658 (Roberts et al. 2002), which overlaps with the EGRET source 3EG J2021+3716 (see Fig. 1). *Chandra* observations of this pulsar detected a $\sim 20'' \times 10''$ pulsar wind nebula named PWN G75.2+0.1 (Hessels et al. 2004). *Chandra* observations of the pulsar and its PWN detected rings and jets around PSR J2021+3651, and inferred a distance to the pulsar of 3–4 kpc (Van Etten et al. 2008), in contrast to the 12 kpc implied by the pulsar dispersion measure (Roberts et al. 2002). *XMM-Newton* observations show emission extending to a distance of ∼10–15 arcminutes, whereas radio observations with the VLA at 1.4 GHz show a radio nebula coincident with the X-ray extension (Roberts et al. 2008).

AGILE detected the source AGL J2020.5+3653 at energies above 100 MeV range, which shows pulsations and was associated with the pulsar PSR J2021+3651 (Halpern et al. 2008). The photon spectrum of the source can be fitted by a power-law of photon index $\Gamma = 1.86 \pm 0.18$ in the range 100–1000 MeV, while a turndown is seen above 1.5 GeV. This source appears as 1AGL J2021+3652 in the first *AGILE* catalog of high confidence gamma-ray sources (Pittori et al. 2009). *Fermi* also detected the source 0FGL 2020.8+3649 in positional coincidence with the pulsar (Abdo et al. 2009).

We found neither a (low-frequency) radio nor a near-infrared source at the position of PSR J2021+3651. The nearest near-infrared source is at a distance of $3''.9$ and has a K_s magnitude of 17.3. In the radio, from our 610 MHz GMRT data we can establish an upper limit to any possible point-like counterpart of 1.0 mJy by multiplying the background emission level by a factor of 5. The radio flux density of the extended emission found with the VLA at 1.4 GHz amounts to ∼700 mJy in an area of about 100 arcmin^2, which for a uniform distribution yields 7 mJy arcmin^{-2}. On the other hand, the rms of our low-resolution radio map at 610 MHz shown in Fig. 1, with a beam size of $30''$, is 0.5 mJy beam^{-1}. This provides a conservative 5-σ upper limit of either 2.5 mJy beam^{-1} or 9 mJy arcmin^{-2}. This upper limit implies that if the radio emission is uniformly distributed, its spectral index must be above -0.3. This value is compatible with the radio emission being produced by the synchrotron mechanism, as expected in this nebula.

6.2. Jet-like radio sources

We discovered two jet-like radio sources located well inside the uncertainty region of MGRO J2019+37. Their J2000.0 positions are $\alpha = 20^{\rm h}18^{\rm m}32^{\rm s}$, $\delta = +37^\circ 02'.5$ (source A) and $\alpha = 20^{\rm h}19^{\rm m}48^{\rm s}$, $\delta = +37^\circ 06'.7$ (source B). In Fig. 3, we show a GMRT high resolution image of each of them superimposed on the near-infrared image. Both sources appear to be unresolved in the NVSS 1.4 GHz catalogue (Condon et al. 1998). Based on our GMRT survey, the NVSS survey, and the Westerbork Northern Sky Survey (WENSS; Rengelink et al. 1997) data at 327 MHz, we estimate a spectral index of -1.16 ± 0.02 for source A, clearly indicating a non-thermal nature. It is interesting to note that the source is not detected in the VLA Low-Frequency Sky Survey (VLSS; Cohen et al. 2007) at 74 MHz, with a 3-σ upper limit of 1.2 Jy. With the spectral index above, we would expect a flux density of 1.9 Jy, clearly indicative of a turnover at lower radio frequencies, which could be produced by intrinsic self-absorption or by Galactic foreground free-free absorption. The GMRT and NVSS data for source B provide a spectral index of -0.7 ± 0.6, compatible with the non-detection in WENSS, and suggesting a non-thermal nature for this radio source.

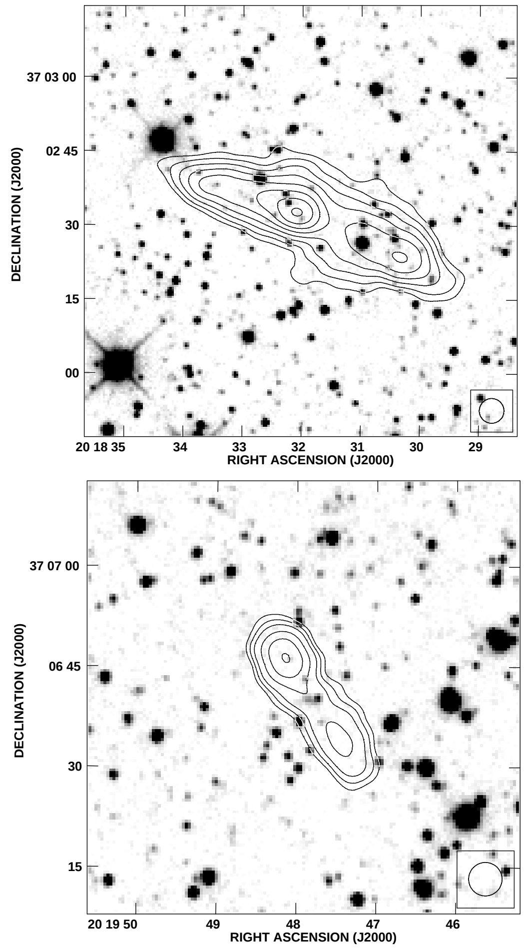

Fig. 3. Radio and near-infrared image composition of the jet-like radio sources A (top) and B (bottom). The GMRT radio contours are superimposed on the K_s-band 3.5 m CAHA telescope images. *Top*: Source A. Contours correspond to 5, 9, 15, 23, 45, 60, and 80 times 0.16 mJy beam^{-1}, the rms noise. The integrated flux density of the source is 164.7 ± 0.3 mJy. *Bottom*: Source B. Contours correspond to 5, 8, 12, 20, 30, and 42 times 0.16 mJy beam^{-1}, which is the rms noise. The integrated flux density of the source is 28 ± 0.1 mJy. The synthesized radio beams of $5''$ are plotted in the lower-right corners of both images.

Source A (Fig. 3-top) shows a double-sided morphology, sources #141 and #142 in Table 2 of the online material, with a slight bending towards the south-east. This structure resembles ones typically seen in radio galaxies with a non-negligible pressure from the intergalactic medium. Unfortunately, there is no clear extended NIR counterpart in the axis joining the radio lobes that could be identified with the parent galaxy, and no firm conclusion can be obtained from the present data.

Source B (Fig. 3-bottom) shows a morphological and spectral similarity to the radio lobes of the ‘great annihilator’

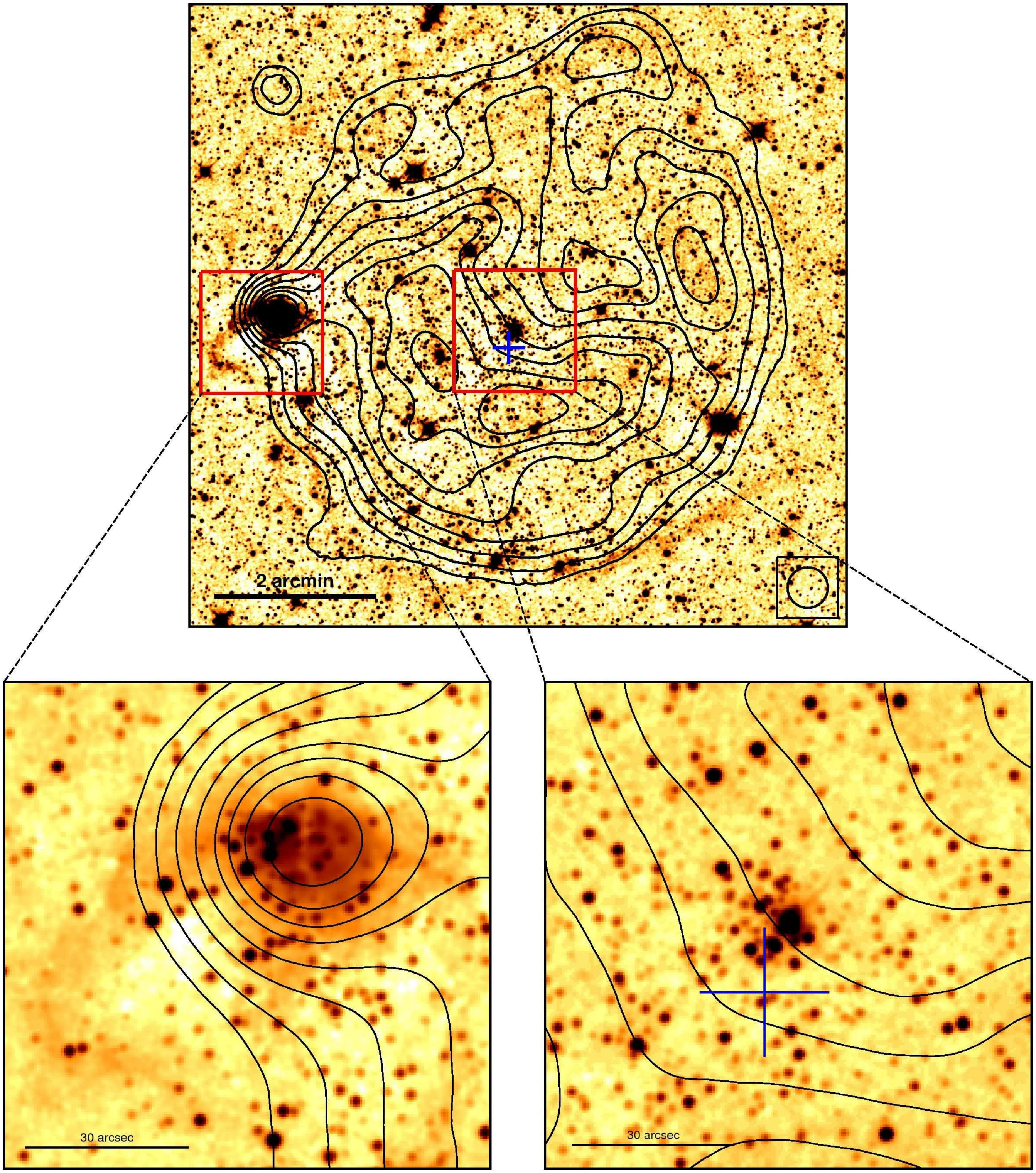

Fig. 4. *Top*: Composite radio and near-infrared image centred on the Sh 2-104 region. The contours correspond to 10, 20, 35, 55, 80, 100, 125, 155 times the rms noise of 0.3 mJy beam^{-1} of our GMRT 610 MHz (49 cm wavelength) image. We overlay our K_s-band near-infrared image of the same field obtained using the 3.5 m telescope at Calar Alto. The blue cross marks the position and 1-σ uncertainty of the *ROSAT* source 2RXP J201742.3+364513. *Bottom-left*: Young massive stellar cluster deeply embedded in a UCHII region found on the eastern rim of Sh 2-104. *Bottom-right*: New cluster candidate in the center of Sh 2-104 previously assumed to be a single star (identified later as 2MASS J20174184+3645264). The scale of each image is indicated by the horizontal bar. The colour scale of the bottom images was changed to display the individual stars within each cluster more clearly.

1E 1740.7−2942, a microquasar at the Galactic center (Mirabel et al. 1992). The two lobes correspond to sources #193 and #194 in Table 2 of the online material. We did not detect a radio core in this source but, as for the one present in 1E 1740.7−2942, it could have a flat spectrum and the flux density at such a low frequency is expected to be very low compared to that of the radio lobes. As can be seen in the figure, there are two near-infrared objects close to the central position of the source. Their J2000.0 coordinates and magnitudes are: α=20$^{\rm h}$19$^{\rm m}$47$\overset{\rm s}{.}$74, δ=+37°06′40$\overset{\prime\prime}{.}$2, $K_{\rm s}$=16.5, and α=20$^{\rm h}$19$^{\rm m}$47$\overset{\rm s}{.}$86, δ=+37°06′39$\overset{\prime\prime}{.}$9, $K_{\rm s}$=17.4. Their proximity significantly biases the photometry. The bright source is point-like and offset from the axis traced by the radio lobes. The faint source is aligned with the axis and fuzzy, implying that the origin of the double radio source is most likely a radio galaxy.

Previous *ROSAT* pointed observations (Obs. Id. 500248P conducted on 24 October 1993) did not detect any of these two radio-jet sources, placing a 3-σ upper limit of 7×10^{-14} erg cm^2 s^{-1} on their persistent flux in the energy range 0.1–2.4 keV. With the present data, we cannot elucidate whether the sources are Galactic or extragalactic, although there are hints of their extragalactic nature.

6.3. H II *region Sh 2-104*

Sh 2-104, also known as Sh 104, is an optically visible H II region of 7′ diameter at a distance of 4.0±0.5 kpc (Deharveng et al. 2003). There is a central O6 V star suspected of being responsible for ionizing the region (Lahulla et al. 1985). The appearance of Sh 2-104 in the optical and in the radio bands is very similar, although the radio images show the presence of an ultra compact H II (UCHII) region at the eastern border, which is not visible in the optical image (Deharveng et al. 2003). The interaction between the expanding H II region Sh 2-104 and the UCHII region may be responsible for triggered star formation in the latter, resulting in a deeply embedded young cluster. This region has also been detected as a high luminosity (3×10^4 L$_\odot$) *IRAS* source.

Our GMRT observations (see Fig. 4) detect a structure similar to that found at 1.46 GHz with the VLA (Fich 1993) and at 1.4 GHz within the NVSS radio continuum survey (Condon et al. 1998).

We also observed Sh 2-104 in the near-infrared $K_{\rm s}$-band. The images obtained are deeper than those from 2MASS. Figure 4 shows our near-infrared images of the field of Sh 2-104 with the radio emission contours superimposed. In the eastern region of the ring (to the left side), the near-infrared image shows the well known cluster associated with the UCHII region, which must contain at least one massive OB star (Deharveng et al. 2003). In the central part of the image, the single O6 V star of Lahulla et al. (1985), which corresponds to 2MASS J20174184+3645264 (Skrutskie et al. 2006), now appears to be resolved as several point-like objects, indicative of the presence of a cluster. Therefore, apart from this ionizing early-type star, the new cluster candidate could also contribute to the formation of the H II region (e.g., additional early type stars, wind shocks). Furthermore, an elongated arc along the south of Sh 2-104 as well as to the east of the UCHII region can be discerned in the NIR images. These features may be related to the interaction between the expanding H II region and the interstellar medium.

Despite its deep coverage at other wavelengths, Sh 2-104 was poorly explored in the X-ray domain. Previous X-ray observations of this region by *ROSAT* detected a source (2RXP J201742.3+364513; Rosat consortium 2000) located at α=20$^{\rm h}$17$^{\rm m}$42$\overset{\rm s}{.}$3, δ=+36°45′13″ with a positional error of ∼12″, overlapping with the central star 2MASS J20174184+3645264 and the cluster candidate (see bottom-right of Fig. 4). The count rate of $(4.1 \pm 0.5) \times 10^{-3}$ count s^{-1} in the energy range 0.1–2.0 keV, provides a flux of $(5.8 \pm 0.7) \times 10^{-14}$ erg cm^{-2} s^{-1} based on the assumption of a thermal spectrum with a temperature of 1.5 keV (a typical value for colliding wind regions). On the other hand, OB stars are known to be X-ray sources, presumably because of shocks in their stellar winds (see Güdel 2004 for a review). According to the complete study by Berghöfer et al. (1997) of more than 200 isolated OB stars detected in *ROSAT* data, for an O6 V star, with bolometric luminosity of 8×10^{38} erg s^{-1} (Martins et al. 2005), the corresponding X-ray luminosity is 1.2×10^{32} erg s^{-1}. Considering a distance of 4.0 kpc to both Sh 2-104 and its ionizing central star 2MASS J20174184+3645264, the expected X-ray flux is 6.3×10^{-14} erg cm^{-2} s^{-1}, fully compatible with the detected X-ray flux from 2RXP J201742.3+364513.

Table 1. Non-simultaneous flux density measurements of the source NVSS J202032+363158 obtained from different surveys.

Survey	Frequency (MHz)	Flux density (mJy)
VLSS	74	6354±708
WENSS	327	1442±216
CGPS	408	1180±360
GMRT	610	833± 56
NVSS	1400	386± 12
GB6	4850	121± 12
87GB	4850	108± 15

6.4. NVSS J202032+363158

The source NVSS J202032+363158 is the brightest compact radio source within the error box of the TeV peak emission of MGRO J2019+37 in our GMRT observations. Its flux density at 610 MHz is 833 mJy and has not been resolved. This source appears in the VLSS at 74 MHz, in the WENSS at 327 MHz, in the CGPS at 408 MHz (Taylor et al. 1996), in the Effelsberg survey of the Cygnus X region at 1420 MHz (Wendker et al. 1991), and in the Green Bank 4.85 GHz northern sky surveys 87GB (Gregory & Condon 1991) and GB6 (Gregory et al. 1996). In Table 1, we summarize the detected flux densities within these surveys, and we plot the corresponding spectrum in Fig. 5. Assuming a stable flux density, the radio spectrum of this source can be described by $S_\nu = (523 \pm 2)$ mJy $[\nu/{\rm GHz}]^{-0.94\pm0.01}$, and it is, therefore, clearly a non-thermal emitter. Despite very low frequencies being sampled, no evidence of the turnover frequency below 1 GHz is obvious from this simple power-law fit.

By inspecting of the NRAO archives, we found a previous VLA snapshot (6 min on source) of this radio source at the 20 cm wavelength in B configuration (providing a nominal synthesized beam of 4″) observed on 25 March 1989. This observation was calibrated using standard AIPS tasks, including phase self-calibration. A uniformly weighted image is shown in Fig. 6-left. As can be seen, this radio source is resolved, displaying a one-sided radio jet extending a few arcsec towards the north, with a core component of ∼250 mJy and a secondary component of about 70 mJy. To enhance the compact structure of the source, we obtained an image for the longest baselines of the same VLA run, using a uv-range of 30–50 kλ. The image, shown in Fig. 6-right, clearly shows a compact core and a secondary component,

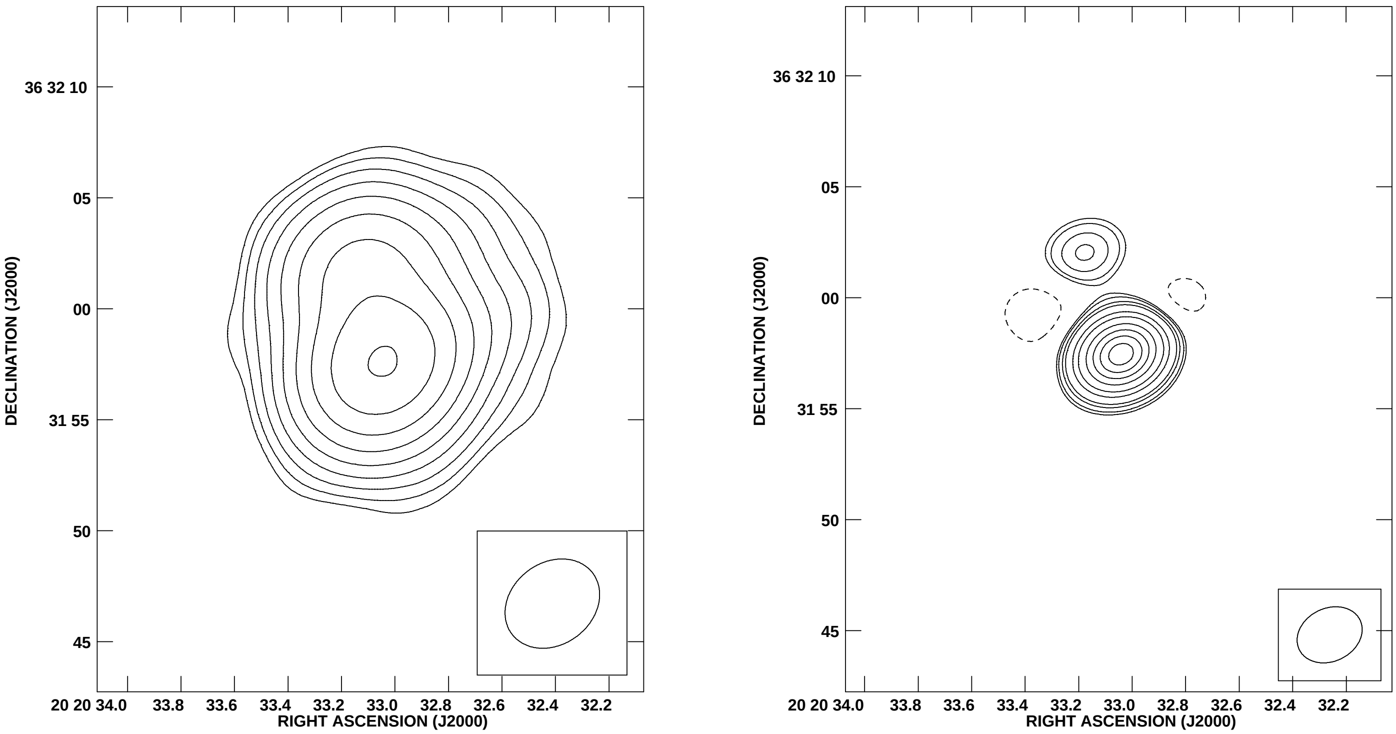

Fig. 6. *(Left)*: Image of the source NVSS J202032+363158 at 21 cm obtained using uniform weights on B-configuration VLA data. The source is resolved, displaying a one-sided radio jet extending a few arc-sec towards the north, with a core component of ∼250 mJy and a secondary component of about 70 mJy. The rms of the image is 0.22 mJy beam^{-1}. Contours correspond to 4, 8, 16, 32, 64, 128, 256, 512, and 1024 times the rms noise. *(Right)*: Image from the same data performed using an *uv*-range of 30–50 kλ, which clearly shows the core and the component discussed in the text, with peak flux densities of 170 and 20 mJy, respectively. The rms of the image is 2.5 mJy beam^{-1}. Contours correspond to −3, 3, 4, 6, 8, 14, 20, 30, 40, 50, and 60 times the rms noise. The synthesized radio beams are plotted in the lower-right corners of both images.

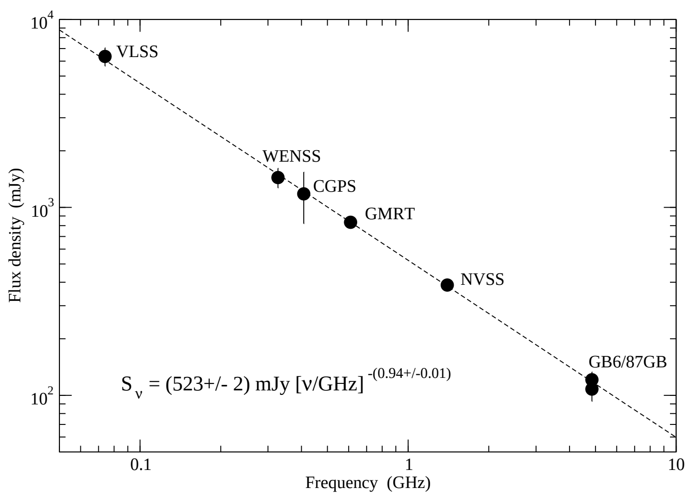

Fig. 5. Radio spectrum of NVSS J202032+363158 based on the flux densities compiled in Table 1. The straight line is a simple power-law fit.

with peak flux densities of 170 and 20 mJy, respectively, resembling the large-scale jet of a microquasar.

To explore the source at higher angular resolutions, we observed the core of NVSS J202032+363158 at 1.6 GHz (18 cm wavelength) with the European VLBI Network in eVLBI mode (eEVN). This is a technique in which the signals from distant radio telescopes are directly streamed into the central data processor for real-time correlation, instead of being recorded on disk or tape. The observation took place on 3 March 2007 from 5:00 to 13:00 UT (centered on MJD 54163.375), and was performed using 6 antennas: Cm, Mc, Jb-2, On-85, Tr, and Wb. Scans on NVSS J202032+363158 were interleaved with scans on the compact phase calibrator J2015+3710, with a 6-min cycle time (66 s on the calibrator and 246 s on the source). The data were recorded using dual polarization and 2-bit sampling, at 256 Mbps. A total bandwidth of 32 MHz per polarization was provided by 4 sub-bands. The e-VLBI data were processed at the Joint Institute for VLBI in Europe (JIVE) correlator in real time, using an integration time of 2 sec. The target source was correlated with the position obtained from the VLA-B (30–50 kλ) data: $\alpha_{\rm J2000.0} = 20^{\rm h}20^{\rm m}33\overset{\rm s}{.}0401$ and $\delta_{\rm J2000.0} = +36°31'57\overset{''}{.}480$, for a total maximum uncertainty of 100 mas. During observations, we experienced synchronization problems and the correlation had to be restarted several times. A few antennas were dropped out of the correlation jobs during the gaps used for measuring the system temperatures. Due to these disconnections, part of the data, which is not recorded onto disks for these experiments, was lost during the correlation, and the true on-source time is estimated to be around 3 hours.

We performed the post-correlation data reduction using the `AIPS` software package and `Difmap`. We applied ionospheric corrections to the visibility data, and the system temperatures were used to obtain the a priori visibility amplitude calibration. All stations produced fringes with the 1-Jy phase calibrator, situated at $1\overset{\circ}{.}2$ from the target, and we therefore transferred the solutions for the phases to the target source. We improved the amplitude calibration using correction factors for each antenna obtained from the self-calibration of J2015+3710. Self-calibration of the NVSS J202032+363158 data was impossible because of the lack of bright sources in the primary beam of the antennas. The phased-referenced natural-weighted image that we obtained had a synthesized beam of 22.7×19.8 mas at a position angle of 30°.3, and an rms noise of 0.20 mJy beam^{-1}. No significant detections were found within a distance of 5″ from the correlated phase center.

There is no near-infrared counterpart candidate to NVSS J202032+363158. The nearest sources are both at 4″.1, with magnitudes of 14.2 and 17.3 in the K_s-band.

7. Could any of the selected individual sources power the TeV emission from MGRO J2019+37?

MGRO J2019+37 covers a sky region of approximately $1° \times 1°$. The extended emission could be produced by either a single powerful accelerator, or by the superposition of several point-like sources. Although we focus on the individual sources presented in Sect. 6, we cannot exclude some of the additional radio sources listed in Table 2 of the online material being responsible for, or contributing to, the Milagro source.

If MGRO J2019+37 is a single extended source, and not a combination of different sources, the origin of the >12 TeV emission is likely to be hadronic. The time required to fill a region of a size of ∼1° (or (1–5)×10^{20} cm at 2–10 kpc distance) with electrons of ∼100 TeV by means of diffusion is

$$t_{\rm diff} = 1.5 \times 10^{12}\, R_{20}^2\, B_{-6}\ \ {\rm s}, \tag{1}$$

where $R_{20} = R/10^{20}$ cm is the source size, and $B_{-6} = B/10^{-6}$ G is the ISM turbulent magnetic field. For realistic ISM densities of $n_{\rm ISM} < 10^4$ cm^{-3}, and reasonable magnetic/mm-far IR field energy densities, i.e., >1 eV cm^{-3}, the electron cooling timescale is dominated by synchrotron and IC losses and found to be $t_{\rm cool} < 10^{11}$ s. Therefore, given that $t_{\rm diff} \gg t_{\rm cool}$, electrons injected from a single accelerator cannot fill the entire multi-TeV source. Otherwise, protons cool mainly by means of collisions with the ISM nuclei (pp)

$$t_{\rm cool} \sim 10^{15}/n_{\rm ISM}\ \ {\rm s}. \tag{2}$$

For $n_{\rm ISM}$ ∼1 000–200 cm^{-3} (2–10 kpc) in the Milagro region, proton injection luminosities of ∼ 10^{37} erg s^{-1} should be enough to explain the observed luminosities (Abdo et al. 2007a) assuming that ∼0.1–1% of the proton power is in >12 TeV photons. As a result of pp interactions, secondary electron-positron pairs and neutrinos are also produced with luminosities and energies similar to those of gamma-rays (e.g., Kelner et al. 2006). These secondary pairs should radiate via synchrotron, relativistic bremsstrahlung, and IC. Extended radio and X-ray emission was detected within the Milagro region (Roberts et al. 2008; Hessels et al. 2004; Van Etten et al. 2008). However, the smaller extent of these diffuse sources compared to the size of the TeV emission makes any possible association difficult. Nevertheless, for typical ISM densities and magnetic and radiation fields, most of the emission from the secondary pairs could be produced at relatively low gamma-ray fluxes, rendering them undetectable.

Once the most probable emission scenario is decided, we will be able to see whether the different objects proposed in Sect. 6 could act as the accelerator.

The spin-down luminosity of PSR J2021+3651 is marginally in agreement with the energetic requirements stated above. Nevertheless, for this object to act as the accelerator, most of this luminosity should be in the form of protons (as in, e.g., Horns et al. 2007b). In addition, the accelerated protons should escape the ∼ 10′ nebula in a time shorter than or equal to the age of the pulsar, ≈ 17 kyr, which may not be possible if the turbulent magnetic field in the nebula reaches value of several 10 μG or higher. On the other hand, the turndown in the *AGILE* GeV spectrum questions the association of AGL J2020.5+3653 as the only counterpart to MGRO J2019+37. Extrapolation of the last two data points in the spectrum shown in Halpern et al. (2008) provide a flux at 20 TeV a factor of 3500 below the reported MGRO J2019+37 flux (Abdo et al. 2007b). Even ignoring the turndown and fitting the entire spectrum with a single power-law, there is still a one order of magnitude difference. Therefore, if no additional components are present in the GeV-TeV spectrum of PSR J2021+3651/PWN G75.2+0.1, this source alone can hardly explain the multi-TeV emission from MGRO J2019+37.

The massive star and the star-forming region (MSR; SFR) associated with the H II region Sh 2-104 could be responsible for the extended Milagro source if they were capable of injecting ∼10^{37} erg s^{-1} in the form of relativistic protons into their surroundings. Assuming an efficiency of a 10% for the kinetic energy converted to non-thermal proton energy in the shocks present inside the H II/SFR region, about 100 massive (proto)stars producing jets or winds with velocities of ∼ 10^8 cm s^{-1} and mass-loss rates of ∼ 10^{-6} $M_\odot$ yr^{-1} would be required to reach the needed proton luminosities. It seems unlikely that Sh 2-104 can harbor such a high number of massive (proto)stars. However, Sh 2-104 may be part of a larger MSR or SFR that have not yet been detected, and in that case, the larger whole MSR or SFR could represent the emitter of the whole Milagro source through wind collisions or jet/medium interactions (see, e.g., Torres et al. 2004; Romero 2008), respectively. In this scenario, thermal free-free radio emission from the whole SFR would be expected. The non-detection of this SFR in our GMRT observations could be explained by free-free absorption in the ionized regions and the surrounding material of the MSR/SFR, although the development of the particular details of this scenario are beyond the scope of this work. Observations searching for maser emission with instruments such as Apex or Nanten could help us to detect this hypothetical star-forming region.

We note that the accelerator itself might be outside MGRO J2019+37, as in the case of the stellar cluster Berkeley 87 mentioned in Abdo et al. (2007a). This cluster could accelerate the protons that would then escape from it diffusing towards, and ultimately interacting with, a denser region located near the Milagro source best-fit model position.

We found three non-thermal radio sources with jet-like structures in the field of MGRO J2019+37: sources A and B, and source NVSS J202032+363158. Although some arguments support the extragalactic nature of sources A and B, we cannot exclude the possibility that they are Galactic in nature. VLBI observations of NVSS J202032+363158 provide an upper limit of 1 mJy beam^{-1} to the flux for a beam size of ∼20 mas. Therefore, this source did not exhibit a compact core during our observations. It was either completely resolved or is a variable radio source, since no radio emission is expected in the high/soft state of microquasars. In any case, these three sources could be hadronic microquasars whose jets would interact with the ISM accelerating protons (e.g., Heinz & Sunyaev 2002; Bordas et al. 2009). The accelerated protons may escape from the accelerating region colliding with the surrounding regions of the ISM, rendering very high-energy emission (e.g., Bosch-Ramon et al. 2005). From the energetic point of view, although these sources could explain the Milagro source, the lack of clear X-ray counterparts needs to be explained, if accretion is taking place in these objects. It might be the case that accretion is inefficient in producing X-rays (as could be the case in LS 5039; e.g., Bosch-Ramon et al. 2007). Finally, a microquasar located outside the Milagro region could be powering the multi-TeV radiation.

The constraint on a hadronic origin for the Milagro emission does not apply if the source consists of different accelerators/emitters. In this case, several leptonic emitters, which may or may not coincide with (some of) the sources discussed here, could be behind MGRO J2019+37.

From this analysis, we conclude that several objects should be considered when trying to understand the origin of MGRO J2019+37, although the nature of the accelerator/emitter remains uncertain. Insights into this question could be provided by further multiwavelength studies, by future imaging atmospheric Cherenkov telescopes (MAGIC-II, H.E.S.S.-II), and by *Fermi*, which should be able to constrain the source position and morphology more tightly, and explore in detail its physics by obtaining spectral information across a broad wavelength range. Finally, neutrino detections with future neutrino instruments could provide additional evidence to support the hadronic scenario.

8. Conclusions

We have carried out a deep radio survey of about 6 square degrees region in the direction of MGRO J2019+37, and a near-infrared survey of the central square degree. This has provided a catalogue of 362 radio sources and a catalogue of 315 000 NIR sources. The radio and NIR data presented here detect a large number of previously unknown sources and shed additional light on known objects. We have found that if a single accelerator is powering MGRO J2019+37, the most likely origin of the multi-TeV emission is hadronic in nature. We have shown that the extrapolation of the spectrum of the pulsar AGL J2020.5+3653 does not explain the detected flux from MGRO J2019+37. This indicates either that there is an additional component in the GeV-TeV spectrum of the pulsar and/or that other sources, such as those discussed here, could contribute to the emission of the Milagro source. The results presented in this paper may be useful in interpreting future data provided by the *Fermi* satellite of the gamma-ray sources in this remarkable region of the Galactic plane. The physical understanding of the most relevant sources in the field is currently a work in progress, in addition to the analysis of new *XMM-Newton* and *AGILE* observations.

Acknowledgements. We thank the staff of the GMRT who have made these observations possible. GMRT is run by the National Centre for Radio Astrophysics of the Tata Institute of Fundamental Research. Based on observations collected at the Centro Astronómico Hispano Alemán (CAHA) at Calar Alto, operated jointly by the Max-Planck Institut für Astronomie and the Instituto de Astrofísica de Andalucía (CSIC) This publication makes use of data products from the Two Micron All Sky Survey, which is a joint project of the University of Massachusetts and the Infrared Processing and Analysis Center/California Institute of Technology, funded by the NASA and NSF in the USA. e-VLBI developments in Europe are supported by the EC DG-INFSO funded Communication Network Developments project 'EXPReS' Contract No. 02662. The European VLBI Network is a joint facility of European, Chinese, South African and other radio astronomy institutes funded by their national research councils. We acknowledge support by DGI of the Spanish Ministerio de Educación y Ciencia (MEC) under grants AYA2007-68034-C03-01, AYA2007-68034-C03-02 and AYA2007-68034-C03-03, FEDER funds and Junta de Andalucía under PAIDI research group FQM-322. J.M. was supported by the Spanish Ministerio de Ciencia e Innovacion (MICINN) under fellowship BES-2008-004564. M.P. and M.R. acknowledge financial support from MEC and European Social Funds through a *Ramón y Cajal* research contract. V.B-R. gratefully acknowledges support from the Alexander von Humboldt Foundation. P.B. was supported by the DGI of MEC (Spain) under fellowship BES-2005-7234. G.E.R is supported by the Argentine Agencies CONICET (PIP 5375) and ANPCyT (PICT 03-13291). We thank the anonymous referee for his useful comments.

References

Abdo, A. A., Allen, B., Berley, D., et al. (The Milagro Collaboration) 2007a, ApJ, 658, L33

Abdo, A. A., Allen, B., Berley, D., et al. (The Milagro Collaboration) 2007b, ApJ, 664, L91

Abdo, A. A., Ackermann, M., Ajello, M., et al. (The *Fermi* LAT Collaboration) 2009, ApJS, submitted, [arXiv:0902.1340v1]

Aharonian, F. A., & Atoyan, A. M. 1996, A&A, 309, 917

Aharonian, F. A., & Atoyan, A. M. 1998, NewAR, 42, 579

Amenomori, M., Ayabe, S., Bi, X. J., et al. 2006, Science, 314, 439

Amenomori, M., Bi, X. J., Chen, D., & et al. 2008, Proceedings of the 30th ICRC, 2, 695

Berghöfer, T. W., Schmitt, J. H. M. M., Danner, R., & Cassinelli, J. P. 1997, A&A, 322, 167

Bertin, E., & Arnouts, S. 1996, A&AS, 117, 393

Bordas, P., Bosch-Ramon, V., Paredes, J. M., & Perucho, M. 2009, A&A, 497, 325

Bosch-Ramon, V., Aharonian, F. E., & Paredes, J. M. 2005, A&A, 432, 609

Bosch-Ramon, V., Motch, C., Ribó, M., et al. 2007, A&A, 473, 545

Butt, Y., Benaglia, P., Combi, J. A., et al. 2003, ApJ, 597, 494

Cohen, A. S., Lane, W. M., Cotton, W. D., et al. 2007, AJ, 134, 1245

Condon, J. J., Cotton, W. D., Greisen, E. W., et al. 1998, AJ, 115, 1693

Deharveng, L., Lefloch, B., Zavagno, A., et al. 2003, A&A, 408, L25

Fich, M. 1993, ApJS, 86, 475

Gregory, P. C., & Condon, J. J. 1991, ApJS, 75, 1011

Gregory, P. C., Scott, W. K., Douglas, K., & Condon, J. J. 1996, ApJS, 103, 427

Güdel, M. 2004, Astron. Astrophys. Review, 12, 71

Halpern, J. P., Gotthelf, E. V., Leighly, K. M., Helfand, D. J. 2001, ApJ, 547, 323

Halpern, J. P., Camilo, F., Giuliani, A., et al. 2008, ApJ, 688, L33

Hartman, R. C., Bertsch, D. L., Bloom, S. D., et al. 1999, ApJS, 123, 79

Heinz, S., & Sunyaev, R. 2002, A&A, 390, 751

Hessels, J. W. T., Roberts, M. S. E., Ransom, S. M., et al. 2004, ApJ, 612, 389

Horns, D., Hoffmann, A. I. D., Santangelo, A., Aharonian, F. A., & Rowell, G. P. 2007a, A&A, 469, L17

Horns, D., Aharonian, F., Hoffmann, A. I. D., & Santangelo, A. 2007b, Ap&SS, 309, 189

Kelner, S. R., Aharonian, F. A., & Bugayov, V. V. 2006, Phys. Rev. D, 74, 4018

Kieda, D. B., et al. 2008, Proceedings of the 30th ICRC, 2, 843

Lahulla, J. F. 1985, A&AS, 61, 537

Lamb, R. C., & Macomb, D. J. 1997, ApJ, 488, 872

Martins, F., Schaerer, D., & Hillier, D. J. 2005, A&A, 436, 1049

Mirabel, I. F., Rodríguez, L. F., Cordier, B., Paul, J., & Lebrun, F. 1992, Nature, 358, 215

Mukherjee, R., Gotthelf, E. V., Halpern, J., & Tavani, M. 2000, ApJ, 542, 740

Paredes, J. M., Martí, J., Ishwara Chandra, C. H., & Bosch-Ramon, V. 2007, ApJ, 654, L135

Paredes, J. M., Martí, J., Ishwara-Chandra, C. H., et al. 2008, A&A, 482, 247

Pittori, C., Verrecchia, F., Chen, A. W., et al. 2009, A&A, submitted, [arXiv:0902.2959v1]

Rengelink, R. B., Tang, Y., de Bruyn, A. G., et al. 1997, A&AS, 124, 259

Roberts, M. S. E., Hessels, J. W. T., Ransom, S. M., et al. 2002, ApJ, 577, L19

Roberts, M. S. E., Brogan, C., Ransom, S., et al. 2008, AIP Conference Series, 1085, 328

Rosat Consortium 2000, VizieR Online Data Catalog, 9030, 0

Romero, G. E. 2008, AIP Conference Series, 1085, 97

Setia Gunawan, D. Y. A., de Bruyn, A. G., van der Hucht, K. A., & Williams, P. M. 2003, ApJS, 149, 123

Skrutskie, M. F., Cutri, R. M., Stiening, R., et al. 2006, AJ, 131, 1163

Taylor, A. R., Goss, W. M., Coleman, P. H., van Leeuwen, J., & Wallace, B. J. 1996, ApJS, 107, 239

Taylor, A. R., Gibson, S. J., Peracaula, M., et al. 2003, AJ, 125, 3145

Torres, D. F., Domingo-Santamaría, E., & Romero, G. E. 2004, ApJ, 601, L75

Van Etten, A., Romani, R. W., & Ng, C.-Y. 2008, ApJ, 680, 1417

Wendker, H. J., Higgs, L. A., & Landecker, T. L. 1991, A&A, 241, 551

Online Material

Table 2. List of GMRT sources detected at 610 MHz, including their names, positions, peak flux densities, integrated flux densities, NIR magnitudes (dots denote that the radio source is outside our NIR mosaic, while ND represents non-detections) and X-ray fluxes (dots imply that the radio source is outside the X-ray fields, while ND stands for non-detections).

#	Name	RA (J2000.0)	DEC (J2000.0)	Peak flux density (mJy beam^{-1})	Local Noise (mJy beam^{-1})	Integrated flux density (mJy)	Error (mJy)	K_s (mag)	$F_{0.2-12\ \mathrm{keV}}$ (erg cm^{-2} s^{-1})
1	GMRT J201142.7+374208	20:11:42.73	+37:42:08.5	8.00	0.53	9.24	0.18	...	ND
2	GMRT J201146.3+364937	20:11:46.38	+36:49:37.5	4.59	0.33	24.81	0.30	...	ND
3	GMRT J201146.5+362243	20:11:46.58	+36:22:43.8	74.05	0.44	136.67	0.24	...	...
4	GMRT J201147.6+362234	20:11:47.62	+36:22:34.2	86.34	0.42	149.12	0.22	...	...
5	GMRT J201201.3+362753	20:12:01.33	+36:27:53.7	12.93	0.37	14.96	0.12	...	...
6	GMRT J201205.7+371130	20:12:05.71	+37:11:30.6	9.14	0.49	17.85	0.30	...	...
7	GMRT J201209.8+361841	20:12:09.85	+36:18:41.2	4.15	0.26	4.51	0.09	...	...
8	GMRT J201210.2+373305	20:12:10.20	+37:33:05.6	7.30	0.37	8.72	0.14	...	...
9	GMRT J201215.7+364050	20:12:15.74	+36:40:50.5	5.55	0.31	6.23	0.12	...	...
10	GMRT J201226.0+364915	20:12:26.09	+36:49:15.3	7.32	0.24	6.98	0.08	...	...
11	GMRT J201231.1+361933	20:12:31.14	+36:19:33.2	39.65	0.23	46.83	0.10	...	...
12	GMRT J201231.9+361939	20:12:31.98	+36:19:39.0	39.07	0.23	45.91	0.10	...	...
13	GMRT J201238.8+362608	20:12:38.86	+36:26:08.8	4.82	0.28	5.10	0.09	...	...
14	GMRT J201239.1+360441	20:12:39.18	+36:04:41.3	8.42	0.19	8.83	0.07	...	...
15	GMRT J201239.2+363457	20:12:39.24	+36:34:57.5	14.63	0.36	40.81	0.24	...	ND
16	GMRT J201239.6+372145	20:12:39.65	+37:21:45.7	11.85	0.40	17.96	0.18	...	...
17	GMRT J201239.7+362538	20:12:39.71	+36:25:38.8	5.06	0.26	5.22	0.08	...	...
18	GMRT J201240.2+363444	20:12:40.26	+36:34:44.0	16.26	0.36	36.98	0.22	...	...
19	GMRT J201242.7+365510	20:12:42.78	+36:55:10.4	11.65	0.24	20.67	0.11	...	...
20	GMRT J201243.7+374416	20:12:43.75	+37:44:16.5	46.67	0.38	54.87	0.16	...	...
21	GMRT J201245.3+363333	20:12:45.39	+36:33:33.1	41.41	0.33	65.06	0.16	...	...
22	GMRT J201246.6+361309	20:12:46.61	+36:13:09.7	4.06	0.23	4.07	0.08	...	...
23	GMRT J201248.2+374332	20:12:48.20	+37:43:32.5	18.02	0.35	19.03	0.12	...	ND
24	GMRT J201300.6+370004	20:13:00.65	+37:00:04.8	4.51	0.26	4.87	0.10	...	...
25	GMRT J201304.5+365736	20:13:04.57	+36:57:36.2	43.73	0.28	69.86	0.13	...	...
26	GMRT J201305.3+365739	20:13:05.35	+36:57:39.4	58.91	0.28	100.44	0.15	...	...
27	GMRT J201305.4+360134	20:13:05.41	+36:01:34.5	21.11	0.22	21.95	0.09	...	ND
28	GMRT J201317.0+370715	20:13:17.03	+37:07:15.8	14.39	0.29	16.44	0.11	...	ND
29	GMRT J201319.6+373729	20:13:19.66	+37:37:29.4	8.81	0.30	9.25	0.12	...	...
30	GMRT J201320.9+375132	20:13:20.94	+37:51:32.4	30.36	0.40	37.25	0.16	...	...
31	GMRT J201324.1+375516	20:13:24.13	+37:55:16.7	10.60	0.45	13.89	0.17	...	...
32	GMRT J201334.0+361501	20:13:34.03	+36:15:01.8	35.94	0.26	82.97	0.15	...	...
33	GMRT J201334.3+360926	20:13:34.33	+36:09:26.0	224.70	0.37	376.50	0.22	...	...
34	GMRT J201337.0+360942	20:13:37.01	+36:09:42.7	54.91	0.38	241.40	0.30	...	...
35	GMRT J201346.1+365908	20:13:46.19	+36:59:08.2	5.20	0.24	5.45	0.08	...	...
36	GMRT J201347.5+365539	20:13:47.56	+36:55:39.4	3.49	0.23	5.49	0.10	...	ND
37	GMRT J201347.7+373920	20:13:47.70	+37:39:20.5	9.85	0.33	13.32	0.14	...	ND
38	GMRT J201349.1+355827	20:13:49.11	+35:58:27.9	6.72	0.26	5.90	0.07	...	...
39	GMRT J201405.5+372431	20:14:05.59	+37:24:31.4	12.58	0.38	15.84	0.15	...	ND
40	GMRT J201408.7+373325	20:14:08.77	+37:33:25.4	28.25	0.37	47.09	0.18	...	...
41	GMRT J201409.4+373400	20:14:09.49	+37:34:00.1	50.56	0.39	74.39	0.19	...	...
42	GMRT J201410.4+371552	20:14:10.48	+37:15:52.8	23.05	0.50	36.08	0.23	...	...
43	GMRT J201410.7+371544	20:14:10.71	+37:15:44.1	14.84	0.50	21.21	0.21	...	...
44	GMRT J201412.4+355218	20:14:12.48	+35:52:18.0	8.82	0.30	16.61	0.15	...	...
45	GMRT J201413.4+355242	20:14:13.45	+35:52:42.7	5.31	0.29	8.41	0.13	...	...
46	GMRT J201416.1+372344	20:14:16.16	+37:23:44.0	7.36	0.42	28.14	0.30	...	...
47	GMRT J201418.2+372339	20:14:18.23	+37:23:39.7	5.58	0.44	13.50	0.19	...	ND
48	GMRT J201425.7+353650	20:14:25.78	+35:36:50.1	14.38	0.34	24.24	0.16	...	...
49	GMRT J201435.8+364550	20:14:35.80	+36:45:50.7	4.49	0.34	13.36	0.18	...	...
50	GMRT J201449.4+374335	20:14:49.45	+37:43:35.1	38.17	0.34	75.05	0.19	...	...
51	GMRT J201450.9+360136	20:14:50.94	+36:01:36.6	95.37	0.39	264.77	0.30	...	...
52	GMRT J201451.6+360149	20:14:51.64	+36:01:49.9	31.94	0.39	138.58	0.30	...	...
53	GMRT J201451.8+370025	20:14:51.82	+37:00:25.6	14.90	0.56	23.33	0.24	...	...
54	GMRT J201452.0+361758	20:14:52.07	+36:17:58.6	13.67	0.33	17.10	0.12	...	...
55	GMRT J201454.4+370034	20:14:54.46	+37:00:34.6	16.24	0.56	25.47	0.21	...	...
56	GMRT J201509.0+373725	20:15:09.05	+37:37:25.0	7.66	0.33	9.47	0.12	...	...
57	GMRT J201509.3+371655	20:15:09.32	+37:16:55.6	17.09	0.88	60.91	0.60	...	...
58	GMRT J201510.6+370049	20:15:10.69	+37:00:49.5	10.73	0.54	21.55	0.30	...	...
59	GMRT J201516.5+362701	20:15:16.52	+36:27:01.5	401.95	0.69	632.20	0.50	...	...
60	GMRT J201517.1+362705	20:15:17.17	+36:27:05.3	294.24	0.69	415.41	0.40	...	ND
61	GMRT J201518.9+353616	20:15:18.91	+35:36:16.1	10.61	0.22	15.70	0.09	...	...
62	GMRT J201527.4+353621	20:15:27.47	+35:36:21.1	22.28	0.25	37.70	0.12	...	...
63	GMRT J201528.7+371100	20:15:28.77	+37:11:00.2	1309.26	1.26	1891.45	0.70	...	...
64	GMRT J201529.7+380119	20:15:29.70	+38:01:19.0	49.27	0.29	74.70	0.15	...	...
65	GMRT J201529.7+363943	20:15:29.71	+36:39:43.5	5.07	0.31	6.63	0.11	...	ND
66	GMRT J201534.7+375728	20:15:34.76	+37:57:28.7	8.19	0.20	29.68	0.17	...	ND
67	GMRT J201535.1+363928	20:15:35.15	+36:39:28.4	3.96	0.30	7.07	0.13	...	...
68	GMRT J201535.5+375718	20:15:35.57	+37:57:18.4	7.11	0.20	50.31	0.30	...	...
69	GMRT J201556.3+365935	20:15:56.35	+36:59:35.6	80.35	0.40	103.09	0.18	...	...
70	GMRT J201557.8+375014	20:15:57.80	+37:50:14.7	7.19	0.17	8.70	0.06	...	...
71	GMRT J201558.1+381003	20:15:58.12	+38:10:03.6	7.62	0.23	10.78	0.10	...	$4.5 \pm 0.1 \times 10^{-13}$
72	GMRT J201558.5+362559	20:15:58.56	+36:25:59.1	31.57	0.26	73.82	0.17	...	...
73	GMRT J201558.7+381004	20:15:58.73	+38:10:04.1	12.22	0.23	23.42	0.13	...	...
74	GMRT J201559.9+362536	20:15:59.90	+36:25:36.8	6.07	0.26	10.12	0.15	...	...
75	GMRT J201600.7+362517	20:16:00.71	+36:25:17.1	13.06	0.26	54.98	0.23	...	...
76	GMRT J201603.2+375721	20:16:03.20	+37:57:21.6	39.66	0.19	58.18	0.10	...	...
77	GMRT J201616.9+353948	20:16:16.95	+35:39:48.4	50.40	0.29	180.26	0.23	...	...
78	GMRT J201619.8+380044	20:16:19.82	+38:00:44.2	3.38	0.16	4.39	0.07	...	...
79	GMRT J201620.9+353945	20:16:20.90	+35:39:45.7	97.32	0.29	314.61	0.21	...	...
80	GMRT J201621.4+354020	20:16:21.41	+35:40:20.6	4.15	0.28	7.07	0.12	...	...

81	GMRT J201621.6+380519	20:16:21.60	+38:05:19.9	2.15	0.18	3.48	0.07	...	...
82	GMRT J201626.0+355829	20:16:26.03	+35:58:29.5	5.76	0.28	8.36	0.12	...	...
83	GMRT J201627.5+365501	20:16:27.51	+36:55:01.1	19.55	0.26	38.45	0.13	...	...
84	GMRT J201641.9+353650	20:16:41.98	+35:36:50.3	48.59	0.28	88.20	0.14	...	...
85	GMRT J201645.3+360034	20:16:45.38	+36:00:34.8	325.22	0.55	698.65	0.40	...	...
86	GMRT J201645.6+360109	20:16:45.66	+36:01:09.7	15.07	0.58	20.37	0.23	...	...
87	GMRT J201646.2+380601	20:16:46.26	+38:06:01.9	2.80	0.17	3.35	0.07	...	...
88	GMRT J201648.2+363133	20:16:48.23	+36:31:33.8	13.05	0.18	44.51	0.13	...	ND
89	GMRT J201654.2+372553	20:16:54.27	+37:25:53.0	15.98	0.41	24.75	0.23	...	...
90	GMRT J201654.4+363104	20:16:54.46	+36:31:04.5	4.44	0.18	9.43	0.11	...	...
91	GMRT J201656.4+371353	20:16:56.46	+37:13:53.8	3.98	0.25	4.93	0.10	...	...
92	GMRT J201657.6+370545	20:16:57.62	+37:05:45.4	6.43	0.21	11.75	0.09	...	...
93	GMRT J201659.9+363231	20:16:59.99	+36:32:31.0	2.76	0.18	2.57	0.06	...	...
94	GMRT J201700.5+360126	20:17:00.52	+36:01:26.3	9.45	0.42	14.53	0.15	...	...
95	GMRT J201700.5+354712	20:17:00.55	+35:47:12.8	11.58	0.27	23.36	0.14	...	...
96	GMRT J201701.5+354654	20:17:01.53	+35:46:54.3	39.87	0.33	87.71	0.19	...	...
97	GMRT J201716.8+375819	20:17:16.83	+37:58:19.3	12.53	0.17	23.37	0.09	...	...
98	GMRT J201720.8+350749	20:17:20.88	+35:07:49.9	5.90	0.34	10.16	0.15	...	...
99	GMRT J201721.9+354610	20:17:21.98	+35:46:10.7	17.31	0.30	47.70	0.17	...	...
100	GMRT J201725.8+373043	20:17:25.88	+37:30:43.1	6.84	0.41	11.19	0.18	...	...
101	GMRT J201726.7+371357	20:17:26.70	+37:13:57.2	9.57	0.19	15.02	0.10	ND	...
102	GMRT J201727.9+355144	20:17:27.97	+35:51:44.1	12.91	0.26	21.93	0.12	...	...
103	GMRT J201732.1+371605	20:17:32.15	+37:16:05.9	3.09	0.19	3.30	0.07	ND	...
104	GMRT J201741.4+355629	20:17:41.42	+35:56:29.3	4.63	0.26	12.86	0.16	...	...
105	GMRT J201742.1+355628	20:17:42.10	+35:56:28.4	3.89	0.26	10.35	0.15	...	...
106	GMRT J201742.1+373507	20:17:42.15	+37:35:07.6	9.83	0.31	14.15	0.15	...	...
107	GMRT J201742.5+372501	20:17:42.55	+37:25:01.8	4.92	0.25	5.06	0.07	...	...
108	GMRT J201744.3+365142	20:17:44.37	+36:51:42.2	5.89	0.16	15.00	0.13	16.0	ND
109	GMRT J201744.8+365045	20:17:44.82	+36:50:45.2	22.12	0.17	33.46	0.08	ND	$5.5 \pm 0.5 \times 10^{-13}$
110	GMRT J201745.4+365315	20:17:45.48	+36:53:15.6	8.61	0.17	14.93	0.09	14.9	ND
111	GMRT J201748.5+371322	20:17:48.58	+37:13:22.2	3.08	0.18	3.57	0.07	ND	...
112	GMRT J201748.6+351833	20:17:48.60	+35:18:33.9	4.10	0.30	5.43	0.11	...	...
113	GMRT J201748.7+375807	20:17:48.76	+37:58:07.0	4.36	0.19	7.02	0.09	...	...
114	GMRT J201749.5+381549	20:17:49.59	+38:15:49.6	206.04	0.48	417.19	0.30	...	...
115	GMRT J201749.9+365508	20:17:49.90	+36:55:08.3	5.11	0.18	6.57	0.08	16.6	$1.0 \pm 0.3 \times 10^{-13}$
116	GMRT J201750.4+370311	20:17:50.48	+37:03:11.3	4.67	0.16	5.18	0.06	ND	...
117	GMRT J201750.5+353407	20:17:50.52	+35:34:07.9	3.11	0.25	3.04	0.07	...	...
118	GMRT J201751.5+351821	20:17:51.51	+35:18:21.6	77.25	0.29	122.32	0.16	...	...
119	GMRT J201753.7+381522	20:17:53.73	+38:15:22.8	7.03	0.46	10.21	0.18	...	...
120	GMRT J201753.8+351822	20:17:53.88	+35:18:22.2	104.31	0.27	189.99	0.17	...	...
121	GMRT J201754.8+375451	20:17:54.84	+37:54:51.5	20.96	0.22	26.22	0.09	...	ND
122	GMRT J201755.1+380017	20:17:55.10	+38:00:17.5	3.13	0.20	5.01	0.09	...	ND
123	GMRT J201756.3+363726	20:17:56.35	+36:37:26.9	11.41	0.25	16.38	0.11	ND	ND
124	GMRT J201756.5+364540	20:17:56.56	+36:45:40.9	15.95	0.20	51.76	0.13	ND	$13.4 \pm 0.7 \times 10^{-13}$
125	GMRT J201756.5+364825	20:17:56.59	+36:48:25.3	12.40	0.16	16.51	0.08	ND	...
126	GMRT J201758.2+370125	20:17:58.29	+37:01:25.3	2.28	0.17	2.57	0.06	13.5	...
127	GMRT J201758.8+351806	20:17:58.83	+35:18:06.3	3.16	0.25	6.00	0.11	...	...
128	GMRT J201759.7+353655	20:17:59.70	+35:36:55.5	14.47	0.28	25.90	0.14	...	...
129	GMRT J201759.7+363018	20:17:59.75	+36:30:18.1	29.44	0.21	39.47	0.09	ND	...
130	GMRT J201803.9+375314	20:18:03.91	+37:53:14.6	4.45	0.22	5.55	0.09	...	...
131	GMRT J201807.4+381436	20:18:07.46	+38:14:36.1	7.84	0.30	9.09	0.10	...	...
132	GMRT J201807.6+360357	20:18:07.64	+36:03:57.2	7.70	0.21	13.11	0.09	...	...
133	GMRT J201808.0+345816	20:18:08.04	+34:58:16.2	12.21	0.39	27.64	0.19	...	...
134	GMRT J201810.1+371936	20:18:10.16	+37:19:36.5	3.11	0.17	8.97	0.08	...	...
135	GMRT J201811.2+354551	20:18:11.25	+35:45:51.1	2.68	0.23	3.77	0.07	...	...
136	GMRT J201812.7+350746	20:18:12.79	+35:07:46.7	5.00	0.21	5.35	0.06	...	...
137	GMRT J201813.0+360046	20:18:13.08	+36:00:46.3	14.58	0.21	19.16	0.10	...	...
138	GMRT J201815.4+352032	20:18:15.45	+35:20:32.5	10.38	0.18	11.18	0.07	...	...
139	GMRT J201822.6+351212	20:18:22.61	+35:12:12.8	4.80	0.19	5.67	0.08	...	ND
140	GMRT J201823.9+370819	20:18:23.94	+37:08:19.4	27.63	0.16	37.99	0.08	ND	...
141	GMRT J201830.6+370225	20:18:30.64	+37:02:25.6	7.55	0.17	61.16	0.20	ND	...
142	GMRT J201832.4+370234	20:18:32.43	+37:02:34.5	13.66	0.16	103.51	0.21	ND	...
143	GMRT J201833.5+374016	20:18:33.53	+37:40:16.7	3.72	0.22	10.24	0.13	...	...
144	GMRT J201834.4+374020	20:18:34.45	+37:40:20.8	9.48	0.22	17.34	0.13	...	...
145	GMRT J201839.3+380853	20:18:39.32	+38:08:53.6	77.29	0.30	269.62	0.21	...	...
146	GMRT J201841.8+361717	20:18:41.86	+36:17:17.8	10.01	0.25	14.25	0.11	...	...
147	GMRT J201842.7+381242	20:18:42.79	+38:12:42.0	72.15	0.25	84.24	0.11	...	...
148	GMRT J201843.7+351006	20:18:43.78	+35:10:06.2	2.39	0.18	2.44	0.06	...	...
149	GMRT J201843.7+381656	20:18:43.79	+38:16:56.6	4.28	0.21	4.23	0.07	...	...
150	GMRT J201844.9+375108	20:18:44.93	+37:51:08.8	5.09	0.21	6.35	0.08	...	...
151	GMRT J201848.4+353512	20:18:48.43	+35:35:12.9	11.20	0.18	12.45	0.07	...	ND
152	GMRT J201848.4+353137	20:18:48.49	+35:31:37.2	4.76	0.16	7.74	0.09	...	...
153	GMRT J201848.5+371937	20:18:48.50	+37:19:37.7	6.76	0.16	8.57	0.08	...	...
154	GMRT J201850.2+351734	20:18:50.24	+35:17:34.7	3.37	0.15	3.64	0.05	...	...
155	GMRT J201850.8+350926	20:18:50.80	+35:09:26.0	5.68	0.18	13.84	0.13	...	...
156	GMRT J201851.6+350930	20:18:51.60	+35:09:30.0	4.02	0.18	8.61	0.10	...	...
157	GMRT J201852.4+363632	20:18:52.46	+36:36:32.0	32.61	0.22	64.00	0.12	ND	...
158	GMRT J201854.0+355023	20:18:54.07	+35:50:23.1	3.83	0.23	3.56	0.07	...	ND
159	GMRT J201854.6+352821	20:18:54.64	+35:28:21.4	5.39	0.16	5.26	0.05	...	...
160	GMRT J201855.5+360213	20:18:55.50	+36:02:13.1	2.54	0.17	2.38	0.06	...	...
161	GMRT J201856.5+360609	20:18:56.58	+36:06:09.9	2.81	0.19	3.08	0.07	...	...
162	GMRT J201858.0+375656	20:18:58.02	+37:56:56.6	2.82	0.23	7.95	0.12	...	...
163	GMRT J201859.5+372451	20:18:59.58	+37:24:51.2	11.17	0.21	16.11	0.09	...	...
164	GMRT J201904.0+370206	20:19:04.04	+37:02:06.6	3.17	0.12	4.57	0.05	ND	...
165	GMRT J201904.8+360809	20:19:04.83	+36:08:09.8	4.86	0.20	4.52	0.07	...	...
166	GMRT J201908.7+374925	20:19:08.78	+37:49:25.8	11.24	0.24	13.52	0.10	...	...
167	GMRT J201913.7+352154	20:19:13.72	+35:21:54.3	49.36	0.20	60.42	0.10	...	...

168	GMRT J201914.5+351518	20:19:14.56	+35:15:18.7	2.28	0.16	4.01	0.07	...	ND
169	GMRT J201914.5+354400	20:19:14.58	+35:44:00.7	58.11	0.25	90.26	0.13	...	...
170	GMRT J201914.6+352156	20:19:14.67	+35:21:56.9	28.84	0.20	43.13	0.10	...	...
171	GMRT J201916.0+373528	20:19:16.03	+37:35:28.5	9.35	0.16	12.51	0.07	...	...
172	GMRT J201916.6+371151	20:19:16.64	+37:11:51.0	2.35	0.12	12.85	0.11	ND	...
173	GMRT J201917.5+373553	20:19:17.51	+37:35:53.9	9.41	0.17	9.13	0.06	...	...
174	GMRT J201918.2+355025	20:19:18.25	+35:50:25.1	18.46	0.23	41.69	0.12	...	...
175	GMRT J201918.3+373828	20:19:18.35	+37:38:28.6	23.21	0.16	25.67	0.07	...	...
176	GMRT J201920.0+363750	20:19:20.04	+36:37:50.5	20.59	0.22	30.44	0.10	16.9	...
177	GMRT J201920.4+380314	20:19:20.48	+38:03:14.7	3.03	0.17	3.04	0.06	...	...
178	GMRT J201920.9+373504	20:19:20.95	+37:35:04.2	2.16	0.17	4.02	0.08	...	...
179	GMRT J201922.0+352227	20:19:22.09	+35:22:27.0	2.17	0.18	2.39	0.06	...	ND
180	GMRT J201925.9+354158	20:19:25.92	+35:41:58.9	34.62	0.25	50.12	0.12	...	...
181	GMRT J201926.9+381656	20:19:26.91	+38:16:56.1	6.35	0.16	6.30	0.06	...	...
182	GMRT J201928.1+362610	20:19:28.11	+36:26:10.4	12.91	0.19	28.06	0.10	15.6	...
183	GMRT J201930.6+375339	20:19:30.62	+37:53:39.8	3.23	0.20	4.16	0.08	...	...
184	GMRT J201931.8+372423	20:19:31.81	+37:24:23.1	4.03	0.16	12.35	0.11	...	...
185	GMRT J201932.3+372440	20:19:32.31	+37:24:40.3	3.10	0.17	9.80	0.11	...	ND
186	GMRT J201933.9+370440	20:19:33.95	+37:04:40.2	34.03	0.14	56.00	0.07	ND	...
187	GMRT J201940.6+350424	20:19:40.67	+35:04:24.4	2.97	0.25	3.35	0.08	...	...
188	GMRT J201941.2+361144	20:19:41.24	+36:11:44.1	11.58	0.26	13.62	0.10	...	...
189	GMRT J201943.2+372956	20:19:43.24	+37:29:56.0	17.74	0.24	24.76	0.10	...	...
190	GMRT J201943.7+353224	20:19:43.70	+35:32:24.3	7.89	0.19	13.47	0.08	...	...
191	GMRT J201943.9+371909	20:19:43.93	+37:19:09.7	4.40	0.14	5.19	0.07	...	...
192	GMRT J201945.4+351826	20:19:45.41	+35:18:26.8	3.13	0.17	2.99	0.06	...	...
193	GMRT J201947.4+370634	20:19:47.47	+37:06:34.3	3.70	0.16	10.88	0.10	ND	...
194	GMRT J201948.1+370645	20:19:48.12	+37:06:45.6	6.85	0.16	17.08	0.11	ND	ND
195	GMRT J201950.2+382949	20:19:50.22	+38:29:49.5	16.78	0.19	19.26	0.07	...	...
196	GMRT J201951.1+362936	20:19:51.13	+36:29:36.3	34.80	0.25	53.50	0.12	ND	...
197	GMRT J201952.4+354727	20:19:52.40	+35:47:27.4	5.07	0.24	6.44	0.09	...	...
198	GMRT J201953.8+350353	20:19:53.87	+35:03:53.6	3.58	0.27	7.45	0.12	...	...
199	GMRT J201955.3+371757	20:19:55.37	+37:17:57.3	7.78	0.13	9.19	0.06	ND	...
200	GMRT J201956.8+373914	20:19:56.84	+37:39:14.3	3.51	0.16	2.94	0.05	...	...
201	GMRT J201958.7+381427	20:19:58.78	+38:14:27.4	2.58	0.15	2.36	0.05	...	...
202	GMRT J201959.2+371833	20:19:59.25	+37:18:33.0	4.93	0.15	10.18	0.09	...	ND
203	GMRT J202000.5+365806	20:20:00.52	+36:58:06.7	2.10	0.13	2.71	0.05	ND	...
204	GMRT J202000.7+351809	20:20:00.74	+35:18:09.7	17.71	0.22	69.92	0.20	...	ND
205	GMRT J202000.9+351829	20:20:00.99	+35:18:29.1	3.16	0.23	21.59	0.19	...	...
206	GMRT J202001.5+351736	20:20:01.51	+35:17:36.3	9.55	0.21	49.79	0.20	...	...
207	GMRT J202003.7+375018	20:20:03.75	+37:50:18.0	54.54	0.23	73.58	0.11	...	...
208	GMRT J202003.9+373135	20:20:03.92	+37:31:35.8	8.21	0.30	17.49	0.17	...	...
209	GMRT J202007.5+352415	20:20:07.57	+35:24:15.5	22.37	0.23	127.83	0.22	...	...
210	GMRT J202008.0+374027	20:20:08.04	+37:40:27.8	4.73	0.18	4.35	0.07	...	...
211	GMRT J202008.4+370147	20:20:08.47	+37:01:47.8	4.59	0.12	6.91	0.07	ND	...
212	GMRT J202010.5+365749	20:20:10.56	+36:57:49.3	2.68	0.14	2.63	0.05	ND	...
213	GMRT J202011.1+362246	20:20:11.16	+36:22:46.1	2.98	0.22	3.96	0.08	...	...
214	GMRT J202011.6+354916	20:20:11.65	+35:49:16.4	3.92	0.23	5.66	0.10	...	ND
215	GMRT J202011.9+362335	20:20:11.97	+36:23:35.7	12.46	0.22	22.50	0.11	...	...
216	GMRT J202012.6+374016	20:20:12.67	+37:40:16.2	2.94	0.18	3.61	0.07	...	...
217	GMRT J202020.2+370059	20:20:20.22	+37:00:59.7	1.65	0.12	1.69	0.04	ND	...
218	GMRT J202020.6+382845	20:20:20.64	+38:28:45.0	3.21	0.18	3.24	0.06	...	...
219	GMRT J202022.0+352459	20:20:22.09	+35:24:59.9	8.46	0.26	20.32	0.15	...	...
220	GMRT J202022.1+372843	20:20:22.11	+37:28:43.0	62.30	0.26	88.20	0.13	...	...
221	GMRT J202026.0+360726	20:20:26.07	+36:07:26.7	35.89	0.35	88.69	0.21	...	ND
222	GMRT J202029.1+364212	20:20:29.10	+36:42:12.5	3.60	0.20	5.08	0.08	ND	...
223	GMRT J202029.6+355131	20:20:29.65	+35:51:31.8	11.72	0.21	19.07	0.10	...	...
224	GMRT J202029.8+353821	20:20:29.81	+35:38:21.1	5.88	0.22	8.48	0.10	...	...
225	GMRT J202033.0+363159	20:20:33.03	+36:31:59.5	421.37	0.43	833.51	0.30	ND	...
226	GMRT J202035.3+363130	20:20:35.32	+36:31:30.2	5.65	0.44	8.35	0.16	ND	ND
227	GMRT J202036.4+373634	20:20:36.43	+37:36:34.9	8.22	0.17	10.24	0.10	...	...
228	GMRT J202038.6+364721	20:20:38.65	+36:47:21.1	4.63	0.18	8.42	0.08	ND	...
229	GMRT J202039.6+352621	20:20:39.64	+35:26:21.0	58.18	0.27	95.75	0.14	...	...
230	GMRT J202040.8+362113	20:20:40.87	+36:21:13.1	8.80	0.20	16.28	0.09	...	...
231	GMRT J202043.9+381811	20:20:43.91	+38:18:11.4	17.22	0.15	26.29	0.08	...	...
232	GMRT J202044.8+354540	20:20:44.87	+35:45:40.9	4.10	0.25	10.66	0.14	...	...
233	GMRT J202046.7+362731	20:20:46.78	+36:27:31.8	4.25	0.33	4.60	0.10	ND	...
234	GMRT J202046.7+370650	20:20:46.79	+37:06:50.0	20.31	0.17	27.76	0.08	ND	...
235	GMRT J202047.6+351429	20:20:47.60	+35:14:29.1	7.24	0.35	26.85	0.30	...	...
236	GMRT J202047.8+353249	20:20:47.85	+35:32:49.8	10.52	0.23	14.88	0.11	...	...
237	GMRT J202048.3+380858	20:20:48.31	+38:08:58.0	45.50	0.18	67.08	0.10	...	...
238	GMRT J202054.3+371120	20:20:54.39	+37:11:20.5	7.91	0.15	12.65	0.08	ND	...
239	GMRT J202055.8+383625	20:20:55.89	+38:36:25.1	37.89	0.35	49.79	0.16	...	...
240	GMRT J202101.6+354028	20:21:01.66	+35:40:28.7	3.75	0.19	4.20	0.07	...	...
241	GMRT J202105.3+382326	20:21:05.39	+38:23:26.0	6.71	0.19	6.92	0.06	...	...
242	GMRT J202106.6+352441	20:21:06.69	+35:24:41.3	10.14	0.26	17.39	0.14	...	...
243	GMRT J202109.3+371446	20:21:09.34	+37:14:46.1	3.49	0.19	4.40	0.06	ND	...
244	GMRT J202116.6+362128	20:21:16.68	+36:21:28.5	5.33	0.19	6.22	0.08	...	...
245	GMRT J202120.1+362229	20:21:20.12	+36:22:29.1	2.66	0.20	2.39	0.06	...	...
246	GMRT J202120.2+352628	20:21:20.24	+35:26:28.1	86.25	0.24	113.62	0.12	...	...
247	GMRT J202121.7+355226	20:21:21.75	+35:52:26.4	4.01	0.26	8.78	0.13	...	...
248	GMRT J202126.9+382542	20:21:26.97	+38:25:42.9	11.76	0.24	13.77	0.09	...	...
249	GMRT J202128.6+354623	20:21:28.62	+35:46:23.1	5.33	0.20	5.90	0.08	...	...
250	GMRT J202131.0+355452	20:21:31.03	+35:54:52.6	14.50	0.24	18.32	0.10	...	...
251	GMRT J202131.1+354706	20:21:31.19	+35:47:06.7	8.45	0.21	8.04	0.07	...	...
252	GMRT J202131.2+354338	20:21:31.24	+35:43:38.1	3.86	0.17	3.56	0.06	...	...
253	GMRT J202133.8+355005	20:21:33.81	+35:50:05.7	209.34	0.27	240.10	0.14	...	...
254	GMRT J202135.6+370950	20:21:35.67	+37:09:50.5	49.01	0.19	104.52	0.13	ND	ND

255	GMRT J202136.0+382122	20:21:36.05	+38:21:22.0	3.12	0.23	2.59	0.07	...	...
256	GMRT J202136.2+380704	20:21:36.26	+38:07:04.3	3.63	0.19	5.10	0.08	...	...
257	GMRT J202136.7+381812	20:21:36.71	+38:18:12.0	3.40	0.24	4.69	0.09	...	...
258	GMRT J202138.4+373110	20:21:38.48	+37:31:10.8	68.13	0.32	3090.77	0.90	...	...
259	GMRT J202141.3+372557	20:21:41.36	+37:25:57.6	54.13	0.53	2866.42	1.50	...	...
260	GMRT J202143.3+353334	20:21:43.34	+35:33:34.1	3.01	0.17	4.06	0.07	...	...
261	GMRT J202147.7+363929	20:21:47.76	+36:39:29.2	37.14	0.24	48.73	0.11	ND	...
262	GMRT J202149.1+373301	20:21:49.13	+37:33:01.6	6.15	0.30	11.48	0.18	...	...
263	GMRT J202149.5+362526	20:21:49.55	+36:25:26.9	8.66	0.21	9.71	0.08	ND	...
264	GMRT J202149.6+364323	20:21:49.60	+36:43:23.0	71.92	0.29	175.73	0.18	ND	...
265	GMRT J202150.4+373014	20:21:50.40	+37:30:14.2	9.00	0.32	48.84	0.40	...	...
266	GMRT J202153.8+355622	20:21:53.84	+35:56:22.7	18.53	0.23	27.50	0.11	...	ND
267	GMRT J202154.4+354339	20:21:54.41	+35:43:39.3	5.05	0.17	4.56	0.06	...	...
268	GMRT J202154.6+374619	20:21:54.62	+37:46:19.2	48.56	0.19	56.53	0.08	...	...
269	GMRT J202158.0+370938	20:21:58.06	+37:09:38.7	2.69	0.23	4.51	0.09	...	...
270	GMRT J202158.4+380651	20:21:58.44	+38:06:51.6	2.52	0.19	3.01	0.07	...	...
271	GMRT J202158.6+354335	20:21:58.66	+35:43:35.7	15.72	0.17	27.36	0.09	...	...
272	GMRT J202201.3+361112	20:22:01.38	+36:11:12.1	51.45	0.24	78.39	0.13	...	...
273	GMRT J202207.8+373006	20:22:07.89	+37:30:06.9	2.28	0.27	5.16	0.10	...	...
274	GMRT J202209.9+352927	20:22:09.98	+35:29:27.6	11.60	0.19	13.90	0.08	...	...
275	GMRT J202210.7+380826	20:22:10.78	+38:08:26.1	5.83	0.22	8.16	0.11	...	...
276	GMRT J202213.2+355940	20:22:13.21	+35:59:40.8	4.23	0.23	5.52	0.09	...	...
277	GMRT J202214.1+370031	20:22:14.10	+37:00:31.4	3.31	0.23	3.44	0.07	...	...
278	GMRT J202216.7+373059	20:22:16.75	+37:30:59.5	4.62	0.24	5.20	0.11	...	...
279	GMRT J202218.7+365421	20:22:18.71	+36:54:21.6	35.30	0.28	56.32	0.13	...	...
280	GMRT J202218.8+362526	20:22:18.86	+36:25:26.6	2.92	0.24	3.17	0.07	...	...
281	GMRT J202220.5+374759	20:22:20.59	+37:47:59.5	30.61	0.15	32.57	0.07	...	...
282	GMRT J202225.1+363138	20:22:25.12	+36:31:38.2	3.73	0.25	4.12	0.09	...	...
283	GMRT J202225.8+355521	20:22:25.83	+35:55:21.7	38.20	0.22	43.09	0.09	...	...
284	GMRT J202230.0+370105	20:22:30.00	+37:01:05.8	5.17	0.24	9.57	0.11	...	...
285	GMRT J202231.6+375537	20:22:31.64	+37:55:37.1	17.90	0.16	24.74	0.07	...	...
286	GMRT J202235.5+351935	20:22:35.59	+35:19:35.6	57.51	0.33	87.06	0.16	...	...
287	GMRT J202236.1+351940	20:22:36.18	+35:19:40.5	14.35	0.33	22.32	0.15	...	...
288	GMRT J202242.1+380342	20:22:42.14	+38:03:42.1	5.23	0.17	5.70	0.06	...	...
289	GMRT J202242.7+353445	20:22:42.73	+35:34:45.3	3.44	0.18	3.43	0.06	...	...
290	GMRT J202242.9+373227	20:22:42.91	+37:32:27.9	3.72	0.23	4.11	0.08	...	...
291	GMRT J202248.9+373927	20:22:48.94	+37:39:27.7	8.79	0.17	8.70	0.06	...	...
292	GMRT J202251.6+353326	20:22:51.67	+35:33:26.4	5.02	0.18	4.89	0.06	...	...
293	GMRT J202258.2+361625	20:22:58.28	+36:16:25.2	7.58	0.19	12.72	0.11	...	...
294	GMRT J202258.5+361147	20:22:58.50	+36:11:47.2	4.62	0.23	4.86	0.08	...	...
295	GMRT J202259.9+375020	20:22:59.95	+37:50:20.4	24.07	0.17	24.95	0.07	...	...
296	GMRT J202303.7+352129	20:23:03.73	+35:21:29.3	99.10	0.37	145.95	0.18	...	...
297	GMRT J202308.0+355829	20:23:08.00	+35:58:29.5	4.90	0.35	5.98	0.12	...	...
298	GMRT J202309.0+373641	20:23:09.09	+37:36:41.1	4.14	0.17	4.15	0.07	...	...
299	GMRT J202313.5+374833	20:23:13.57	+37:48:33.5	95.36	0.20	133.27	0.10	...	...
300	GMRT J202319.3+351811	20:23:19.35	+35:18:11.5	26.57	0.46	38.88	0.20	...	...
301	GMRT J202320.8+362834	20:23:20.83	+36:28:34.3	6.87	0.20	18.72	0.15	...	...
302	GMRT J202329.2+375111	20:23:29.29	+37:51:11.3	4.45	0.16	4.98	0.06	...	...
303	GMRT J202329.9+371530	20:23:29.96	+37:15:30.1	9.06	0.19	10.03	0.09	...	...
304	GMRT J202339.9+355100	20:23:39.94	+35:51:00.2	55.50	0.33	79.15	0.15	...	...
305	GMRT J202345.3+372731	20:23:45.35	+37:27:31.8	13.46	0.23	19.61	0.10	...	...
306	GMRT J202347.8+373425	20:23:47.83	+37:34:25.4	8.91	0.21	10.22	0.08	...	...
307	GMRT J202351.4+375343	20:23:51.44	+37:53:43.9	4.04	0.16	3.78	0.06	...	...
308	GMRT J202355.0+373810	20:23:55.03	+37:38:10.0	50.73	0.22	249.27	0.18	...	...
309	GMRT J202403.3+360803	20:24:03.38	+36:08:03.8	4.32	0.30	7.94	0.14	...	...
310	GMRT J202404.2+380216	20:24:04.20	+38:02:16.4	8.05	0.21	7.21	0.07	...	...
311	GMRT J202404.2+374300	20:24:04.29	+37:43:00.6	30.30	0.18	93.28	0.13	...	...
312	GMRT J202407.1+360032	20:24:07.17	+36:00:32.7	9.59	0.42	12.26	0.18	...	...
313	GMRT J202415.5+360821	20:24:15.57	+36:08:21.1	6.93	0.30	8.63	0.13	...	...
314	GMRT J202420.6+355043	20:24:20.60	+35:50:43.6	3.76	0.34	7.61	0.13	...	...
315	GMRT J202422.3+365518	20:24:22.37	+36:55:18.0	45.56	0.27	62.30	0.12	...	...
316	GMRT J202422.6+355354	20:24:22.60	+35:53:54.8	9.21	0.32	9.06	0.11	...	...
317	GMRT J202424.6+373354	20:24:24.67	+37:33:54.3	10.12	0.20	13.81	0.10	...	...
318	GMRT J202430.6+364604	20:24:30.60	+36:46:04.1	20.59	0.25	50.61	0.16	...	...
319	GMRT J202431.0+365139	20:24:31.00	+36:51:39.0	10.79	0.26	16.51	0.11	...	...
320	GMRT J202431.7+363020	20:24:31.73	+36:30:20.0	19.59	0.36	35.91	0.21	...	...
321	GMRT J202432.0+372355	20:24:32.00	+37:23:55.0	11.04	0.24	15.61	0.11	...	...
322	GMRT J202432.0+363012	20:24:32.03	+36:30:12.1	74.10	0.36	121.98	0.20	...	...
323	GMRT J202446.1+370236	20:24:46.12	+37:02:36.2	4.04	0.28	8.03	0.13	...	...
324	GMRT J202450.0+361706	20:24:50.02	+36:17:06.2	4.76	0.39	4.42	0.11	...	...
325	GMRT J202450.7+370300	20:24:50.74	+37:03:00.8	16.17	0.28	40.96	0.17	...	...
326	GMRT J202454.1+361501	20:24:54.13	+36:15:01.6	20.39	0.41	40.35	0.20	...	...
327	GMRT J202455.3+375744	20:24:55.33	+37:57:44.8	10.70	0.33	12.62	0.11	...	...
328	GMRT J202504.3+370312	20:25:04.35	+37:03:12.4	4.08	0.27	6.65	0.12	...	...
329	GMRT J202505.1+370256	20:25:05.18	+37:02:56.0	4.02	0.26	5.06	0.10	...	...
330	GMRT J202508.4+362535	20:25:08.42	+36:25:35.4	8.16	0.46	10.36	0.17	...	...
331	GMRT J202509.4+353642	20:25:09.45	+35:36:42.5	8.96	0.52	47.92	0.50	...	...
332	GMRT J202515.9+370916	20:25:15.91	+37:09:16.8	22.68	0.28	25.20	0.11	...	...
333	GMRT J202523.5+372901	20:25:23.59	+37:29:01.5	43.45	0.18	48.67	0.08	...	...
334	GMRT J202523.6+372314	20:25:23.61	+37:23:14.8	34.09	0.17	1033.75	0.50	...	...
335	GMRT J202532.1+354459	20:25:32.14	+35:44:59.8	4.59	0.32	5.35	0.12	...	...
336	GMRT J202538.5+372024	20:25:38.50	+37:20:24.9	2.69	0.14	2.88	0.06	...	...
337	GMRT J202542.3+374942	20:25:42.36	+37:49:42.4	5.18	0.42	6.55	0.13	...	...
338	GMRT J202543.5+370607	20:25:43.57	+37:06:07.2	6.42	0.26	6.32	0.08	...	...
339	GMRT J202543.6+374917	20:25:43.67	+37:49:17.5	10.20	0.40	15.01	0.15	...	...
340	GMRT J202555.7+361553	20:25:55.73	+36:15:53.9	6.17	0.42	7.03	0.16	...	...
341	GMRT J202556.3+365011	20:25:56.38	+36:50:11.4	5.15	0.21	4.42	0.06	...	...

342	GMRT J202603.5+363628	20:26:03.59	+36:36:28.7	24.43	0.26	25.51	0.10	...	...
343	GMRT J202605.9+361108	20:26:05.97	+36:11:08.3	10.66	0.43	10.25	0.12	...	...
344	GMRT J202608.3+360111	20:26:08.38	+36:01:11.1	7.62	0.32	12.67	0.15	...	...
345	GMRT J202611.1+372845	20:26:11.14	+37:28:45.6	7.54	0.16	10.10	0.10	...	...
346	GMRT J202616.7+360053	20:26:16.72	+36:00:53.2	5.42	0.34	7.58	0.14	...	...
347	GMRT J202625.8+365929	20:26:25.85	+36:59:29.6	6.84	0.27	10.33	0.13	...	ND
348	GMRT J202625.9+365319	20:26:25.90	+36:53:19.1	5.64	0.25	5.82	0.11	...	$1.9 \pm 0.4 \times 10^{-14}$
349	GMRT J202626.8+363712	20:26:26.87	+36:37:12.6	5.32	0.25	5.82	0.09	...	...
350	GMRT J202629.6+370513	20:26:29.65	+37:05:13.6	5.56	0.29	5.94	0.09	...	...
351	GMRT J202632.8+371147	20:26:32.80	+37:11:47.6	2.54	0.20	2.52	0.06	...	...
352	GMRT J202638.4+370730	20:26:38.42	+37:07:30.1	9.79	0.24	6.07	0.08	...	...
353	GMRT J202638.8+370728	20:26:38.84	+37:07:28.1	16.74	0.30	41.84	0.20	...	...
354	GMRT J202645.0+370022	20:26:45.04	+37:00:22.1	42.16	0.32	57.57	0.14	...	...
355	GMRT J202647.2+370613	20:26:47.23	+37:06:13.3	4.88	0.32	9.50	0.16	...	...
356	GMRT J202703.3+374853	20:27:03.33	+37:48:53.5	70.63	0.48	99.53	0.21	...	...
357	GMRT J202712.4+365818	20:27:12.44	+36:58:18.8	8.85	0.48	10.46	0.19	...	...
358	GMRT J202724.8+371042	20:27:24.88	+37:10:42.6	48.80	0.38	89.73	0.20	...	ND
359	GMRT J202727.3+372258	20:27:27.32	+37:22:58.4	72.93	0.50	5013.70	1.40	...	ND
360	GMRT J202730.3+371523	20:27:30.31	+37:15:23.2	10.13	0.32	14.10	0.17	...	...
361	GMRT J202733.3+373116	20:27:33.32	+37:31:16.7	4.32	0.30	25.96	0.30	...	...
362	GMRT J202735.0+373124	20:27:35.00	+37:31:24.6	5.64	0.31	13.32	0.18	...	...

List of Objects

‘MGRO J2019+37’ on page 1
‘MGRO J2019+37’ on page 1
‘AGL J2020.5+3653’ on page 1
‘PSR J2021+3651’ on page 1
‘MGRO J2019+37’ on page 1
‘MGRO J2019+37’ on page 1
‘MGRO J2019+37’ on page 1
‘MGRO J2019+37’ on page 1
‘MGRO J2019+37’ on page 1
‘PSR J2021+3651’ on page 1
‘PWN G75.2+0.1’ on page 1
‘Sh 2-104’ on page 1
‘NVSS J202032+363158’ on page 1
‘PSR J2021+3651’ on page 1
‘AGL J2020.5+3653’ on page 1
‘PWN G75.2+0.1’ on page 1
‘MGRO J2019+37’ on page 1
‘TeV J2032+4130’ on page 1
‘MGRO J2019+37’ on page 2
‘MGRO J2019+37’ on page 2
‘MGRO J2019+37’ on page 2
‘MGRO J2019+37’ on page 2
‘MGRO J2019+37’ on page 2
‘3EG J2021+3716’ on page 2
‘3EG J2016+3657’ on page 2
‘MGRO J2019+37’ on page 2
‘3EG J2021+3716’ on page 2
‘PSR J2021+3651’ on page 2
‘MGRO J2019+37’ on page 2
‘MGRO J2019+37’ on page 2
‘MGRO J2019+37’ on page 2
‘MGRO J2019+37’ on page 2
‘MGRO J2019+37’ on page 2
‘3C 286’ on page 2
‘3C 48’ on page 2
‘J2052+365’ on page 2
‘MGRO J2019+37’ on page 3
‘Sh 2-104’ on page 3
‘NVSS J202032+363158’ on page 3
‘3EG J2021+3716’ on page 3
‘3EG J2016+3657’ on page 3
‘GeV J2020+3658’ on page 3
‘PWN G75.2+0.1’ on page 3
‘B2013+370’ on page 3
‘3EG J2016+3657’ on page 3
‘MGRO J2019+37’ on page 3
‘MGRO J2019+37’ on page 3
‘3EG J2016+3657’ on page 3
‘3EG J2021+3716’ on page 3
‘B2013+370’ on page 3
‘G74.87+1.22’ on page 3
‘MGRO J2019+37’ on page 3
‘PWN G75.2+0.1’ on page 3
‘MGRO J2019+37’ on page 3
‘NVSS J202032+363158’ on page 3
‘Sh 2-104’ on page 3
‘Sh 104’ on page 4
‘MGRO J2019+37’ on page 4
‘MGRO J2019+37’ on page 5
‘PSR J2021+3651’ on page 5
‘PWN G75.2+0.1’ on page 5
‘PSR J2021+3651’ on page 5
‘GeV 2020+3658’ on page 5
‘3EG J2021+3716’ on page 5
‘PWN G75.2+0.1’ on page 5
‘PSR J2021+3651’ on page 5
‘AGL J2020.5+3653’ on page 5
‘PSR J2021+3651’ on page 5
‘1AGL J2021+3652’ on page 5
‘0FGL 2020.8+3649’ on page 5
‘PSR J2021+3651’ on page 5
‘MGRO J2019+37’ on page 5
‘Sh 2-104’ on page 6
‘2RXP J201742.3+364513’ on page 6
‘Sh 2-104’ on page 6
‘Sh 2-104’ on page 6
‘2MASS J20174184+3645264’ on page 6
‘1E 1740.7−2942’ on page 7
‘1E 1740.7−2942’ on page 7
‘Sh 2-104’ on page 7
‘Sh 2-104’ on page 7
‘Sh 104’ on page 7
‘Sh 2-104’ on page 7
‘Sh 2-104’ on page 7
‘Sh 2-104’ on page 7
‘Sh 2-104’ on page 7
‘2MASS J20174184+3645264’ on page 7
‘Sh 2-104’ on page 7
‘Sh 2-104’ on page 7
‘2RXP J201742.3+364513’ on page 7
‘NVSS J202032+363158’ on page 7
‘2MASS J20174184+3645264’ on page 7
‘Sh 2-104’ on page 7
‘2MASS J20174184+3645264’ on page 7
‘2RXP J201742.3+364513’ on page 7
‘NVSS J202032+363158’ on page 7
‘NVSS J202032+363158’ on page 7
‘MGRO J2019+37’ on page 7
‘NVSS J202032+363158’ on page 8
‘NVSS J202032+363158’ on page 8
‘NVSS J202032+363158’ on page 8
‘NVSS J202032+363158’ on page 8
‘NVSS J202032+363158’ on page 8
‘NVSS J202032+363158’ on page 9
‘MGRO J2019+37’ on page 9
‘MGRO J2019+37’ on page 9
‘MGRO J2019+37’ on page 9
‘PSR J2021+3651’ on page 9
‘AGL J2020.5+3653’ on page 9
‘MGRO J2019+37’ on page 9
‘MGRO J2019+37’ on page 9
‘PSR J2021+3651’ on page 9
‘PWN G75.2+0.1’ on page 9
‘MGRO J2019+37’ on page 9
‘Sh 2-104’ on page 9
‘Sh 2-104’ on page 9
‘Sh 2-104’ on page 9
‘MGRO J2019+37’ on page 9
‘Berkeley 87’ on page 9
‘MGRO J2019+37’ on page 9
‘NVSS J202032+363158’ on page 9
‘NVSS J202032+363158’ on page 9
‘LS 5039’ on page 9
‘MGRO J2019+37’ on page 10
‘MGRO J2019+37’ on page 10
‘MGRO J2019+37’ on page 10

'MGRO J2019+37' on page 10
'AGL J2020.5+3653' on page 10
'MGRO J2019+37' on page 10